

SECURITY CLASSIFICATION OF THIS PAGE (When Data Entered)

1

REPORT DOCUMENTATION PAGE

READ INSTRUCTIONS
BEFORE COMPLETING FORM

1. REPORT NUMBER AFIT/CI/NR 88- 35		2. GOVT ACCESSION NO.	3. RECIPIENT'S CATALOG NUMBER
4. TITLE (and Subtitle) THE USE OF THE Q-VECTOR IN OPERATIONAL METEOROLOGY		5. TYPE OF REPORT & PERIOD COVERED MS THESIS	
7. AUTHOR(s) CHARLES ARTHUR LEMAY		6. PERFORMING ORG. REPORT NUMBER	
9. PERFORMING ORGANIZATION NAME AND ADDRESS AFIT STUDENT AT: TEXAS A & M UNIVERSITY		8. CONTRACT OR GRANT NUMBER(s)	
11. CONTROLLING OFFICE NAME AND ADDRESS		10. PROGRAM ELEMENT, PROJECT, TASK AREA & WORK UNIT NUMBERS	
		12. REPORT DATE 1988	
		13. NUMBER OF PAGES 69	
14. MONITORING AGENCY NAME & ADDRESS (if different from Controlling Office) AFIT/NR Wright-Patterson AFB OH 45433-6583		15. SECURITY CLASS. (of this report) UNCLASSIFIED	
		15a. DECLASSIFICATION/DOWNGRADING SCHEDULE	
16. DISTRIBUTION STATEMENT (of this Report) DISTRIBUTED UNLIMITED: APPROVED FOR PUBLIC RELEASE			
17. DISTRIBUTION STATEMENT (of the abstract entered in Block 20, if different from Report) SAME AS REPORT			
18. SUPPLEMENTARY NOTES Approved for Public Release: IAW AFR 190-1 LYNN E. WOLAVER Dean for Research and Professional Development Air Force Institute of Technology Wright-Patterson AFB OH 45433-6583 18 Feb 89			
19. KEY WORDS (Continue on reverse side if necessary and identify by block number) METEOROLOGY			
20. ABSTRACT (Continue on reverse side if necessary and identify by block number) ATTACHED			

DTIC
ELECTE
AUG 02 1988
S D

AD-A196 410

ABSTRACT

The Use of the Q-vector in Operational Meteorology. (May 1988)

Charles Arthur LeMay, B.S., Baptist College

Chair of Advisory Committee: Dr. Dušan Djurić

Evaluation of atmospheric vertical motion is now possible on widely available and inexpensive microcomputers. Using the Q-vector form of the omega equation, formulated by Hoskins et al. (1978) allows a meteorologist to evaluate vertical motion throughout the atmosphere.

Case studies are presented, using an enhanced version of the Barnes (1985) computer program. The first case study deals with a severe weather situation that resulted in tornadic activity through eastern Texas. The second case study covers a two day period in which a Mesoscale Convective Complex (MCC) moved through the central plains states. Results of these case studies show that the Q-vector form of the omega equation is a useful tool for evaluating vertical motion and aids in checking the initialization of the prognostic numerical models. The diagnostic charts, from this program, are available one to two hours before other commonly used charts are produced. Program results are best interpreted on meso and synoptic scales; however, the diagnostic results are best used when incorporated with other routinely available charts. A drawback to the program is that non-geostrophic effects such as orographic influences and friction are not included.

For new literature, n. d. es. 1988.



Accession For	
NTIS CRA&I	<input checked="" type="checkbox"/>
DTIC TAB	<input type="checkbox"/>
Unannounced	<input type="checkbox"/>
Justification	
by	
Date	
Event/Notes	
A-1	

THE USE OF THE Q-VECTOR IN OPERATIONAL METEOROLOGY

A Thesis

by

CHARLES ARTHUR LEMAY

Submitted to the Graduate College of
Texas A&M University
in partial fulfillment of the requirements for the degree of
MASTER OF SCIENCE

May 1988

Major Subject: Meteorology

THE USE OF THE Q-VECTOR IN OPERATIONAL METEOROLOGY

A Thesis

by

CHARLES ARTHUR LEMAY

Approved as to style and content by:

Dusan Djuric

Dušan Djurić
(Chairman of Committee)

Kenneth C. Brundidge

Kenneth C. Brundidge
(Member)

John M. Klinck

John M. Klinck
(Member)

James R. Scoggins

James R. Scoggins
(Head of Department)

May 1988

ABSTRACT

The Use of the Q-vector in Operational Meteorology. (May 1988)

Charles Arthur LeMay, B.S., Baptist College

Chair of Advisory Committee: Dr. Dušan Djurić

Evaluation of atmospheric vertical motion is now possible on widely available and inexpensive micro-computers. Using the Q-vector form of the omega equation, formulated by Hoskins et al. (1978) allows a meteorologist to evaluate vertical motion throughout the atmosphere.

Case studies are presented, using an enhanced version of the Barnes (1985) computer program. The first case study deals with a severe weather situation that resulted in tornadic activity through eastern Texas. The second case study covers a two day period in which a Mesoscale Convective Complex (MCC) moved through the central plains states. Results of these case studies show that the Q-vector form of the omega equation is a useful tool for evaluating vertical motion and aids in checking the initialization of the prognostic numerical models. The diagnostic charts, from this program, are available one to two hours before other commonly used charts are produced. Program results are best interpreted on meso and synoptic scales; however, the diagnostic results are best used when incorporated with other routinely available charts. A drawback to the program is that non-geostrophic effects such as orographic influences and friction are not included.

ACKNOWLEDGEMENTS

I wish to acknowledge first, the United States Air Force for giving me the opportunity to return to Texas A&M University to complete a Masters Degree program. Second I wish to acknowledge my committee chairman, Dr. Dušan Djurić. He inspired me to further my knowledge in all areas, as well as initiating my interest in numerical modelling. He is always willing to help and most important of all he has been a friend during both of my periods at this university. I would also like to acknowledge my other committee members, Dr. Kenneth Brundidge and Dr. John Klinck. Their guidance has enabled me to make my time in graduate school much more productive. All three committee members have shown me how to dig for the answers when I've had questions. Finally I would like to acknowledge Stanley Barnes, a research scientist with the NOAA Environmental Research Laboratory. *He provided the Q-vector program that I have used in my research.* This has saved me countless hours of programming and debugging time and allowed me to concentrate more on research.

TABLE OF CONTENTS

	Page
ABSTRACT	iii
ACKNOWLEDGEMENTS	iv
TABLE OF CONTENTS	v
LIST OF TABLES	vi
LIST OF FIGURES	vii
CHAPTER I. INTRODUCTION	1
CHAPTER II. VERTICAL MOTION EQUATIONS	4
PHYSICAL INTERPRETATION OF Q	9
CHAPTER III. A THREE LEVEL Q -VECTOR PROGRAM	13
CHAPTER IV. CASE STUDIES	25
THUNDERSTORMS IN TEXAS ON 17 MARCH 1987	25
THUNDERSTORMS IN THE CENTRAL PLAINS ON 4 JUNE 1980	49
CHAPTER V. CONCLUSIONS	64
REFERENCES	67
VITA	69

LIST OF TABLES

TABLE	Page
1. Ratios of precipitation points with lifting over total precipitation points and the ratios of precipitation free subsidence points over total subsidence points for 1200 UTC 17 March 1987	46
2. Percentages for data in TABLE 1.	46
3. Ratio of number of precipitation points within lifting regions to total number of lifting points for 1200 UTC 17 March 1987	47
4. Percentages for data in TABLE 3.	47
5. Ratio of precipitation points with lifting over total number of precipitation points for case 2	59
6. Percentages for data in TABLE 5.	60
7. Ratio of number of subsidence points that are precipitation free over the total number of subsidence points for case 2	61
8. Percentages for data in TABLE 7.	61
9. $\nabla \cdot \mathbf{Q} \leq 0$ versus precipitation	62
10. Percentages for data in TABLE 9.	62
11. $\nabla \cdot \mathbf{Q} \leq -2 * 10^{-17} s^{-3} mb^{-1}$ versus precipitation	63
12. Percentages for data in TABLE 11.	63

LIST OF FIGURES

FIGURE	Page
1. Q , horizontal shear case	9
2. Q , confluent case	10
3. Frontogenetic circulation	11
4. Frontolytic circulation	11
5. LFM/TDL grid numbering system	16
6. 850 mb height and temperature for 1200 UTC 17 March 1987	26
7. 700 mb height and temperature for 1200 UTC 17 March 1987	27
8. 500 mb height and temperature for 1200 UTC 17 March 1987	27
9. 300 mb height and temperature for 1200 UTC 17 March 1987	28
10. 600 mb vorticity and 700-500 thickness for 0000 UTC 17 March 1987	30
11. 600 mb vorticity and 700-500 thickness for 1200 UTC 17 March 1987	30
12. 500 mb geopotential tendency for 0000 UTC 17 March 1987	31
13. 700 mb geopotential tendency for 0000 UTC 17 March 1987	32
14. 500 mb geopotential tendency for 1200 UTC 17 March 1987 ..	32
15. 700 mb geopotential tendency for 1200 UTC 17 March 1987	33
16. 800 mb $\nabla \cdot Q$ for 1200 UTC 17 March 1987	34
17. 600 mb $\nabla \cdot Q$ for 1200 UTC 17 March 1987	34
18. 400 mb $\nabla \cdot Q$ for 1200 UTC 17 March 1987	35
19. 850 mb mixing ratio for 0000 UTC 17 March 1987	36
20. 850 mb mixing ratio for 1200 UTC 17 March 1987	36
21. 700 mb mixing ratio for 0000 UTC 17 March 1987	37
22. 700 mb mixing ratio for 1200 UTC 17 March 1987	37

FIGURE

Page

23. 500 mb mixing ratio for 0000 UTC 17 March 1987	38
24. 500 mb mixing ratio for 1200 UTC 17 March 1987	38
25. 800 mb Q and temperature for 1200 UTC 17 March 1987	40
26. 600 mb Q and temperature for 1200 UTC 17 March 1987	41
27. 400 mb Q and temperature for 1200 UTC 17 March 1987	41
28. 800 mb GFF for 1200 UTC 17 March 1987	42
29. 600 mb GFF for 1200 UTC 17 March 1987	42
30. 400 mb GFF for 1200 UTC 17 March 1987	43
31. Composite chart for 1200 UTC 17 March 1987	44
32. 850 mb wind field and surface frontal position for 0000 UTC 4 June 1980	50
33. 800 mb Q and temperature for 0000 UTC 4 June 1980	51
34. 800 mb $\nabla \cdot Q$ for 0000 UTC 4 June 1980	51
35. 600 mb $\nabla \cdot Q$ for 0000 UTC 4 June 1980	52
36. 800 mb GFF for 0000 UTC 4 June 1980	53
37. 800 mb Q and temperature for 1200 UTC 4 June 1980	54
38. 800 mb $\nabla \cdot Q$ for 1200 UTC 4 June 1980	54
39. 800 mb GFF for 1200 UTC 4 June 1980	55
40. 800 mb Q and temperature for 0000 UTC 5 June 1980	56
41. 800 mb $\nabla \cdot Q$ for 0000 UTC 5 June 1980	56
42. 800 mb GFF for 0000 UTC 5 June 1980	57
43. Composite chart for 0000 UTC 4 June 1980	58

CHAPTER I

INTRODUCTION

Before the operational meteorologist can make his next forecast he must examine all the information available and then begin the process of determining what factors will be responsible for the weather during the forecast period. Some of the information available comes in the form of computer generated forecasts for different atmospheric processes. One of the important prognostic products is the vertical velocity chart produced by numerical models such as the Nested Grid Model (NGM) and its predecessor, the Limited area Fine mesh Model (LFM).

Vertical motion in the atmosphere has a pronounced effect upon the weather. Upward motion produces clouds, cyclones, fronts, precipitation, and, in general, destabilization of the atmosphere. Downward motion produces anticyclones and, in general, clearing conditions. The current prognostic product depicting vertical motion is the 700 mb vertical velocity chart. A question here is, what can be done to improve the methods for evaluating atmospheric vertical motion.

The classical omega equation is one possible diagnostic equation that can be used to determine vertical motion. The two forcing terms for vertical motion, in the omega equation, are 1) the vertical derivative of vorticity advection and 2) the horizontal Laplacian of temperature advection. Although these two terms can be associated with separate physical processes, they often have a degree of cancellation

The journal style used is from *Journal of the Atmospheric Sciences*.

between them. Due to a series of approximations in the derivation of the omega equation, the resultant vertical motion is applicable only when the atmosphere is in a state of hydrostatic and geostrophic balance. The results are best used in the middle troposphere.

In the 1940's the evaluation of vertical motion equations was approached from two different viewpoints according to Hoskins et al. (1978). They stated that Sutcliffe produced his theory of development from a diagnostic point of view while Charney extended his theory of baroclinic instability (dynamic point of view).

Sutcliffe (1947), in his development, neglected terms involving the deformation of the wind field. These terms, as Sutcliffe pointed out, can be important in frontal regions as well as in jet entrance and exit regions. Therefore, in large deformation regions such as frontal zones Sutcliffe's approximations are less applicable.

As stated above, the classical omega equation has a drawback in that the vorticity and temperature terms can be misleading when isolated in order to determine their relative magnitude or the resulting sign of vertical motion. This is partly due to the vorticity term being a vertical derivative and the temperature term being determined on a horizontal plane. The two terms are not independent. Trenberth (1978) showed that the vorticity and temperature terms can be expressed with a common term between them. This common term is the advection of vorticity by the thermal wind. In the vorticity term, the common term is a positive quantity while in the temperature term it is a negative quantity. Thus, the two terms have a degree of cancellation between them.

In this thesis a modified version of the omega diagnostic equation will be presented along the lines indicated by Hoskins and his collaborators (Hoskins, Draghici, and Davies 1978) that overcomes these problem areas. It will provide

a determination of vertical motion fields based upon the divergence of a quantity called the Q-vector. A three level numerical model (Barnes 1985) that uses this new vertical motion equation will be discussed. Case studies using the model will be shown in order to determine the model's usefulness as an enhanced tool for operational meteorologists.

The usefulness will be partly determined by making two sets of comparisons. The first comparison will be to see if precipitation, as depicted by the National Weather Service (NWS) Radar Summary chart, is occurring in a area of computed upward vertical motion. This will be done by overlaying the Radar Summary charts onto the 800, 600, and 400 mb $\nabla \cdot \mathbf{Q}$ charts. A second comparison will be to see how much of the computed subsidence areas is precipitation free. Both sets of comparisons will be overlaid onto a grid marked in 1° increments. Results in each set of comparisons will be shown as a set of percentages for each level.

Durran and Snellman (1987) as well as Doswell (1987) have presented arguments for the use of the Q-vector form of the omega equation. These authors agree that it is the best way to evaluate vertical motion numerically.

CHAPTER II

VERTICAL MOTION EQUATIONS

Hoskins, Draghici, and Davies (1978, hereafter HDD) published a new derivation of the omega equation that included the terms that Sutcliffe omitted in his derivation. They derived a one-term representation for the geostrophic determination of ageostrophic motion. From their derivation, the synoptic distribution of vertical motion can be determined from a height and temperature field as given on a constant pressure chart. Hoskins and Pedder (1980) demonstrated that this new method of deriving vertical motion can provide more information than the Sutcliffe equation in describing details of synoptic system development especially when dealing with the horizontal ageostrophic field and intense frontal circulations.

The derivation given by HDD used a vertical coordinate $z = (\theta_0 C_p / g)(1 - (p/p_0)^\kappa)$. The basic equations are:

$$\begin{aligned}\frac{du}{dt} &= fv - \frac{\partial \phi}{\partial x}, \\ \frac{dv}{dt} &= -fu - \frac{\partial \phi}{\partial y}, \\ \frac{d\theta}{dt} &= 0, \\ \frac{\partial u}{\partial x} + \frac{\partial v}{\partial y} + \frac{\partial w}{\partial z} &= 0, \\ \text{and } \frac{\partial \phi}{\partial z} &= \left(\frac{g}{\theta_0} \right) \theta\end{aligned}$$

where θ_0 and P_0 are standard values of potential temperature and pressure, R is the gas constant, $\kappa = R/C_p$, f is the Coriolis parameter and assumed to be constant,

and ϕ is the geopotential. All other symbols represent their standard meteorological meanings.

The geostrophic wind components are:

$$u_g = -\frac{1}{f} \frac{\partial \phi}{\partial y} \quad \text{and} \quad v_g = \frac{1}{f} \frac{\partial \phi}{\partial x}.$$

The thermal wind relations are:

$$-f \frac{\partial u_g}{\partial z} = \frac{g}{\theta_0} \frac{\partial \theta}{\partial y} \quad \text{and} \quad f \frac{\partial v_g}{\partial z} = \frac{g}{\theta_0} \frac{\partial \theta}{\partial x}. \quad (1)$$

The geostrophic vertical component of relative vorticity is:

$$\zeta_g = \frac{\partial v_g}{\partial x} - \frac{\partial u_g}{\partial y}. \quad (2)$$

Taking the vertical derivative of (2), and then substituting the geostrophic terms from (1) into the result yields

$$f \frac{\partial \zeta_g}{\partial z} = \frac{g}{\theta_0} \left(\frac{\partial^2 \theta}{\partial x^2} + \frac{\partial^2 \theta}{\partial y^2} \right) = \frac{g}{\theta_0} \nabla^2 \theta. \quad (3)$$

Now using the quasi-geostrophic form of the vorticity equation,

$$\left(\frac{\partial}{\partial t} + \mathbf{V}_g \cdot \nabla \right) \zeta_g = f \frac{\partial w}{\partial z},$$

taking its vertical derivative, multiplying through by f , and substituting from (3) produces the equation

$$\frac{g}{\theta_0} \frac{\partial}{\partial t} \nabla^2 \theta + f \frac{\partial}{\partial z} (\mathbf{V}_g \cdot \nabla \zeta_g) - f^2 \frac{\partial^2 w}{\partial z^2} = 0. \quad (4)$$

The quasi-geostrophic and adiabatic form of the First Law of Thermodynamics is given as

$$\left(\frac{\partial}{\partial t} + \mathbf{V}_g \cdot \nabla \right) \theta = -w \frac{d}{dz} \Theta \quad (5)$$

where $\Theta(z)$ is the potential temperature.

Multiplying (5) by $(g/\theta_0)\nabla^2$ yields

$$\frac{g}{\theta_0} \frac{\partial}{\partial t} \nabla^2 \theta + \frac{g}{\theta_0} \nabla^2 (\mathbf{V}_g \cdot \nabla \theta) + N^2 \nabla^2 w = 0 \quad (6)$$

where $N^2 = (g/\theta_0)(d\Theta/dz)$ is the squared buoyancy frequency and is assumed to be independent of x and y in this derivation.

Eliminating the time derivative between (4) and (6) produces

$$N^2 \nabla^2 w + f^2 \frac{\partial^2 w}{\partial z^2} = f \frac{\partial}{\partial z} (\mathbf{V}_g \cdot \nabla \zeta_g) - \frac{g}{\theta_0} \nabla^2 (\mathbf{V}_g \cdot \nabla \theta), \quad (7)$$

which is the usual form of the omega equation. This equation shows that the vertical motion is a result of the vertical derivative of vorticity advection and the horizontal Laplacian of thermal advection.

In his derivation of a vertical motion equation, Sutcliffe neglected adiabatic cooling and warming; therefore the $N^2 \nabla^2 w$ term did not appear on the left hand side of (7). The forcing on the right hand side of the equation was reduced to one term at the expense of part of the horizontal Laplacian of thermal advection.

A new version of the omega equation is derived, as described in HDD, by first multiplying the second equation of motion through by f and taking the vertical derivative. The result is

$$\frac{\partial}{\partial t} \left(f \frac{\partial v_g}{\partial z} \right) + \mathbf{V}_g \cdot \nabla f \frac{\partial v_g}{\partial z} + f \frac{\partial \mathbf{V}_g}{\partial z} \cdot \nabla v_g + f^2 \frac{\partial u_{ag}}{\partial z} = 0.$$

Now the term

$$f \frac{\partial \mathbf{V}_g}{\partial z} \cdot \nabla v_g = f \frac{\partial u_g}{\partial z} \frac{\partial v_g}{\partial x} + f \frac{\partial v_g}{\partial z} \frac{\partial v_g}{\partial y}$$

can be rewritten using the continuity equation as

$$f \frac{\partial \mathbf{V}_g}{\partial z} \cdot \nabla v = f \frac{\partial u_g}{\partial z} \frac{\partial v}{\partial x} - f \frac{\partial v_g}{\partial z} \frac{\partial u}{\partial x}.$$

By substituting the thermal wind components (1) it follows that

$$f \frac{\partial \mathbf{V}_g}{\partial z} \cdot \nabla v = -\frac{g}{\theta_0} \left(\frac{\partial \mathbf{V}_g}{\partial x} \cdot \nabla \theta \right) = Q_1.$$

Therefore the second equation of motion can be written as

$$\left(\frac{\partial}{\partial t} + \mathbf{V}_g \cdot \nabla \right) f \frac{\partial v_g}{\partial z} + Q_1 + f^2 \frac{\partial u_{ag}}{\partial z} = 0. \quad (8)$$

Using the thermal equation and multiplying through by g/θ_0 and then taking the x derivative the result is

$$\frac{\partial}{\partial t} \left(\frac{g}{\theta_0} \frac{\partial \theta}{\partial x} \right) + \frac{g}{\theta_0} \frac{\partial \mathbf{V}_g}{\partial x} \cdot \nabla \theta + \frac{g}{\theta_0} \mathbf{V}_g \cdot \nabla \frac{\partial \theta}{\partial x} + \frac{g}{\theta_0} \frac{\partial \theta}{\partial z} \frac{\partial w}{\partial x} = 0.$$

The following substitutions can be made:

$$\begin{aligned} \frac{g}{\theta_0} \frac{\partial \theta}{\partial x} &= f \frac{\partial v_g}{\partial z}, \\ \frac{g}{\theta_0} \frac{\partial \mathbf{V}_g}{\partial x} \cdot \nabla \theta &= -Q_1, \\ \frac{g}{\theta_0} \mathbf{V}_g \cdot \nabla \frac{\partial \theta}{\partial x} &= \mathbf{V}_g \cdot \nabla \left(f \frac{\partial v_g}{\partial z} \right), \\ \text{and } \frac{g}{\theta_0} \frac{\partial \theta}{\partial z} \frac{\partial w}{\partial x} &= N^2 \frac{\partial w}{\partial x}. \end{aligned}$$

Thus the thermal wind equation can be rewritten as

$$\frac{\partial}{\partial t} \left(f \frac{\partial v_g}{\partial z} \right) - Q_1 + \mathbf{V}_g \cdot \nabla \left(f \frac{\partial v_g}{\partial z} \right) + N^2 \frac{\partial w}{\partial x} = 0. \quad (9)$$

In (8) it is seen that the vertical shear of the ageostrophic wind component, u_{ag} , makes a contribution to local change of the horizontal gradient of potential temperature. In (9), the horizontal gradient of potential temperature is affected by the horizontal variation of w .

Eliminating the time derivative in (8) and (9) by subtracting (8) from (9) yields

$$2Q_1 = N^2 \frac{\partial w}{\partial x} - f^2 \frac{\partial u_{ag}}{\partial z}. \quad (10)$$

As seen in (10), Q_1 depends on the horizontal variation of vertical motion and the vertical shear of ageostrophic motion in the x direction. This helps to maintain the thermal wind balance.

By similar arguments it can be shown that

$$2Q_2 = N^2 \frac{\partial w}{\partial y} - f^2 \frac{\partial v_{ag}}{\partial z}. \quad (11)$$

Taking the x derivative of (10), the y derivative of (11), and adding the two resultant equations produces the vertical velocity equation

$$N^2 \nabla^2 w + f^2 \frac{\partial^2 w}{\partial z^2} = 2 \nabla \cdot \mathbf{Q} \quad (12)$$

where

$$\mathbf{Q} = (Q_1, Q_2) = \left(-\frac{g}{\theta_0} \frac{\partial \mathbf{V}_g}{\partial x} \cdot \nabla \theta, -\frac{g}{\theta_0} \frac{\partial \mathbf{V}_g}{\partial y} \cdot \nabla \theta \right).$$

The left hand side of (12) is identical to the left hand side of (7) which is the usual form of the omega equation. The right hand side is now a single forcing term commonly referred to as the divergence of the Q-vector.

Quasi-geostrophic vertical motion is a result of the tendency for advection by the geostrophic wind to destroy thermal wind balance. In reality the atmosphere is never really far from thermal wind balance. The balance is continually reestablished by ageostrophic circulations. Hoskins and Pedder (1980) showed that the Q-vector provides an approximate picture of the ageostrophic horizontal wind in the lower branch of the circulation that develops in order to maintain thermal wind balance in evolving synoptic disturbances. In quasi-geostrophic theory, on an f-plane (Coriolis parameter is held constant) the vertical velocity is determined by the divergence of Q.

PHYSICAL INTERPRETATION OF Q

In order to see the physical significance of Q we can assume a rectangular cartesian coordinate system with the x axis tangential to the potential temperature at the point where the value of Q is to be determined. The y axis will point towards the colder air. In this case $\partial\theta/\partial x = 0$ and the Q -vector components become

$$Q_1 = -\frac{g}{\theta_0} \frac{\partial v_g}{\partial x} \frac{\partial\theta}{\partial y}$$

and $Q_2 = -\frac{g}{\theta_0} \frac{\partial v_g}{\partial y} \frac{\partial\theta}{\partial y}$.

Now Q_1 is related to the horizontal shear and Q_2 to the confluence or diffluence of the geostrophic motion. This is illustrated in Fig. 1 and Fig. 2. As was stated above, the potential temperature is only a function of y in both of these figures.

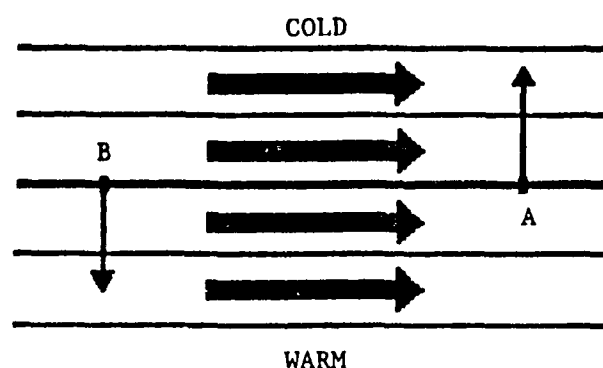


FIG. 1. Q , horizontal shear case. Here v_g is increasing with x . The heavy arrows represent Q and show that Q_1 is positive while $Q_2 = 0$. The y component of motion (thin arrows) is positive at A and negative at B.

The magnitude of Q in each case is inversely proportional to the spacing of the potential temperature contours and directly proportional to the gradient of the v

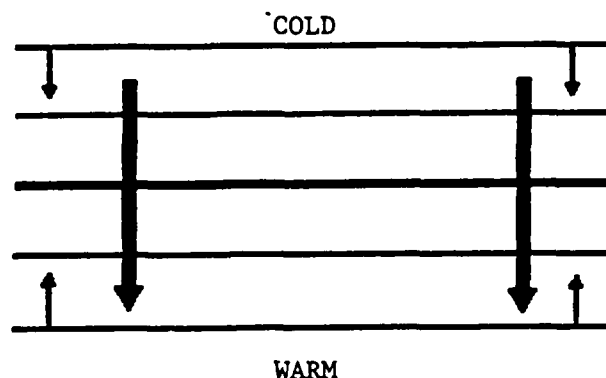


FIG. 2. Q , confluent case. In this case v_g is decreasing with y . The heavy arrows represent Q and show $Q_1 = 0$ and that Q_2 is negative. The y component of motion (thin arrows) is negative in the cold air and positive in the warm air.

component of geostrophic motion. This can be written as $Q \propto (1/L)\nabla v_g$ where L is the spacing of the θ contours.

From the original omega equation $\omega > 0$ implies descent while $\omega < 0$ implies ascent. Equation (12) then shows that $\nabla \cdot Q > 0$ corresponds to descending motion while $\nabla \cdot Q < 0$ is related to ascending motion. Assuming that Q is negligible outside points A and B then in Fig. 1, at point A, the northward moving air should be ascending while the southward moving air, at point B, is descending. If we were to draw streamlines on the figure then we would see Q in a trough. Thus we have rising motion ahead of the trough and subsidence behind the trough. As is the case in the omega equation, rising motion can be associated with positive vorticity advection and subsidence with negative vorticity advection.

Figure 2 shows a confluent case with v_g decreasing with y . In this figure it is assumed that Q is negligible to the north and south of the Q -vectors drawn. Then this figure shows that the southward moving air is subsiding in the cold region and is associated with divergence of Q while the northward moving air is ascending in

the warm sector ($\nabla \cdot \mathbf{Q} < 0$).

In each case the \mathbf{Q} -vector is pointing toward the area with rising motion. This is also shown in Figs. 3 and 4 which depict frontogenetic and frontolytic situations respectively. Figures 3 and 4 assume that the magnitude of the \mathbf{Q} -vector is negligible to the left and right sides of the \mathbf{Q} -vector drawn.

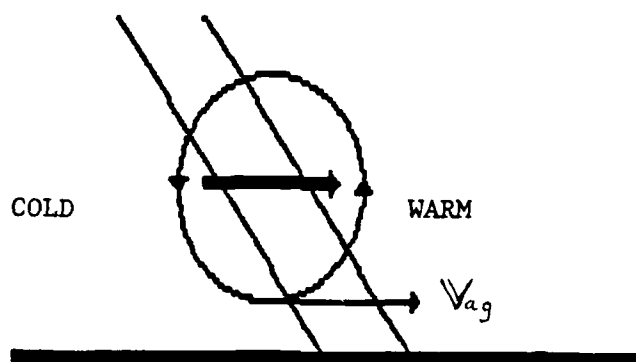


FIG. 3. Frontogenetic circulation. Slanted lines represent a frontal boundary. Heavy arrows represent \mathbf{Q} . Small arrows represent the ageostrophic circulation.

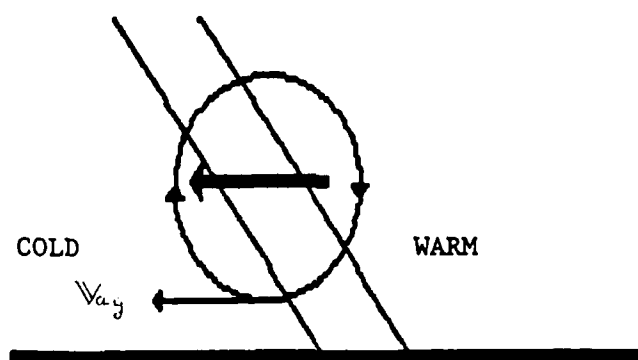


FIG. 4. Frontolytic circulation. Slanted lines represent a frontal boundary. Heavy arrows represent \mathbf{Q} . Small arrows represent the ageostrophic circulation.

In Fig. 3 the geostrophic field tends to intensify the temperature gradient and the direction of \mathbf{Q} is toward warmer air. The low level ageostrophic flow that is

established to maintain the thermal wind balance is towards the warm side. The cross frontal circulation, in this case, has the warm air rising ahead of the front and cold air subsiding behind the front. This is a typical frontogenetic circulation pattern.

Figure 4 shows the opposite case with the temperature gradient being weakened and the cross frontal circulation implying frontolysis. There is warm air subsiding and cold air rising.

It may be noticed that in both Fig. 3 and Fig. 4 that the Q is pointing in the same direction as the low level ageostrophic motion. Having a chart of Q then gives a vectorial representation of horizontal ageostrophic motion below the level at which Q is computed. The same chart then gives some indication of the intensity of the frontal circulation. Having a map of Q superimposed over a temperature field can then show where $\nabla\theta$ is being enhanced or weakened and thus give a picture of system development.

From the above discussion it can be seen that having a chart depicting Q (or a chart of $\nabla \cdot Q$) shows more than just vertical motion. We can more readily see frontal circulations and their corresponding effects as to whether a front has the tendency to strengthen or not. The Q -vector includes terms that were neglected by vertical velocity charts currently in use. Thus the Q -vector form of the omega equation gives a more complete representation of the quasi-geostrophic forcing of vertical motion than the traditional isobaric maps.

CHAPTER III

A THREE LEVEL Q-VECTOR PROGRAM

Cahir, Norman, and Lowry (1981) applied the Q-vector formulation to a summer time cold front moving across the Great Lakes. This was done as part of a demonstration of a real time computer graphics system that could be implemented for operational forecasting purposes. The demonstration only implemented the Q-vector formulation for the 700 mb level and the authors found that the ascent forced by quasi-geostrophic dynamics was spatially related to the cold front.

Barnes (1985) carried the Q-vector formulation further by introducing a two-level model. He used reported height data at mandatory pressure levels to compute contoured patterns of vertical motion and other diagnostic tools at the two levels. The model was applied to a severe convective storm over eastern Colorado that resulted in the development of a mesoscale convective complex (MCC).

For the Barnes' case the LFM/MOS and quantitative precipitation guidance indicated that eastern Wyoming and western Nebraska as the most threatened area, whereas the actual convection was most intense in Colorado. The resulting MCC propagated into Kansas and weakened. Another convective system developed in northeastern New Mexico and moved into the Texas panhandle while intensifying. Barnes' Q-vector diagnostics correctly showed the favorable, for storm development, large scale forcing over eastern Colorado and also over northeastern New Mexico 4 h before the observed changes in the convective systems. According to Barnes, the LFM guidance showed that the Kansas storm would have the most favorable large scale forcing for development and thus was in contradiction with his results.

Barnes has since enhanced his model to produce three levels of contoured diagnostic maps. Through personal communication a micro-computer version of his model has been obtained. The program takes approximately 8 min, on a 8MHz IBM AT class machine, to produce 20 diagnostic maps. This time does not include the data ingest time which, for this study, takes about 5 min using a modem to download data from the Texas A&M Meteorology Department's Harris computer. The required data for the model are the 850, 700, 500, and 300 mb geopotential height, temperature, and dew point depression.

The remainder of this section will deal with the structure of Barnes' three level model and some of the significant algorithms used. The results of using this model will be presented in the case study section of this thesis.

The Barnes' program produces much more than maps of Q , $\nabla \cdot Q$, and a geostrophic frontogenetic function (GFF). GFF is the tendency (moving with the geostrophic motion) for frontogenesis or frontolysis to occur and is evaluated by determining the component of the Q -vector along the potential temperature gradient (i.e., $GFF \propto Q \cdot \nabla \theta$). The model also produces lapse rate of temperature, mixing ratio, height contours, temperature advection, thickness, vorticity, and different types of stability maps among others. At the user's discretion, 20 additional maps can be contoured and the program can easily be modified to produce other desired maps.

The program, as written by Barnes, is in BASIC and can be rewritten in FORTRAN if the need arises. The only problem may be in rewriting the graphics output. Linkable graphics routines, such as the National Center for Atmospheric Research (NCAR) graphics package, would have to be used since FORTRAN doesn't implement any primitive graphics routines. The description of the model is partly

extracted from the information received with the program and also from "dissecting" the provided code.

The model was developed to perform calculations on a portion of the National Meteorological Center's (NMC) LFM grid that is used at the Techniques Development Laboratory (TDL). The LFM grid is cartesian with $\Delta X = \Delta Y = 190.5$ km oriented along 105° W longitude. The origin of the grid is near the southwest corner of the North American continent (see point 1,1 in Fig. 5). The TDL grid is a 31 by 24 portion of the LFM grid and begins at LFM point (15, 8). The model uses a 18 by 15 portion of the grid and the position of the grid is user selectable. The grid and map background must be selected before running the model for the first time or if a new grid portion is desired. The origin of the diagnostic grid is the northwest corner and the north-south grid points are numbered decreasing northward.

The map background is polar stereographic. For output to the screen the coordinates of political and natural space boundaries are determined from latitude-longitude coordinates contained in an external file supplied with the program. After the user enters the northwest corner, the geographic location of the grid is determined and drawn. Station location symbols are then plotted on the map. This map forms the background for all the contoured fields generated by the model.

The northwest corner grid coordinates are then passed to linked programs that calculate the station's location relative to the grid and then determines the radii of the ten closest stations from each grid point. Stations are selected automatically from a list of North American rawinsonde stations, and those selected are located inside of or within one mesh length outside the boundary of the 18 by 15 grid.

The ten smallest radii to stations at each grid point are then passed to another program which determines the influence of each station's observation according to

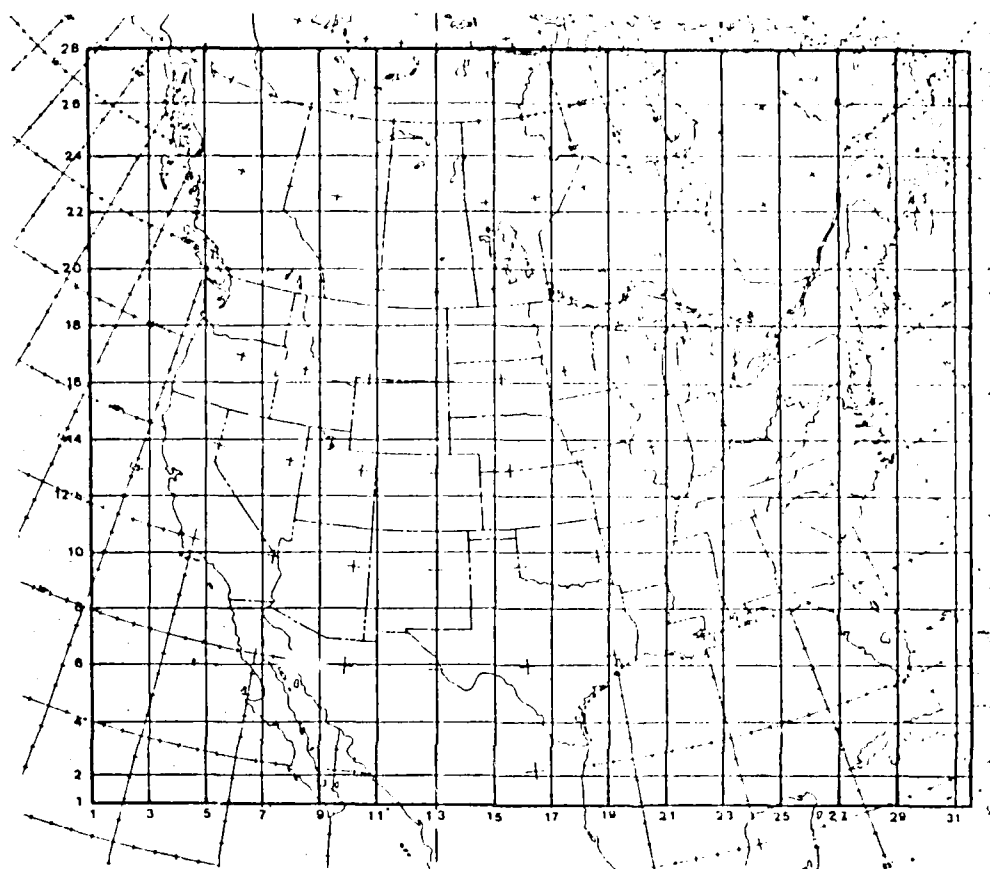


FIG. 5. LFM TDL grid numbering system. Alternate grid points shown. Polar stereographic projection exact at 60°N . LFM mesh size is 190.5 km.

a weighting function which has the form of a Gaussian curve. The final preliminary program computes the Coriolis parameter and the map scaling factor at each grid point.

Data availability and ingest are the most severe constraints upon the operational implementation of the model diagnostics. As stated before, the sounding data required for the omega diagnostics are geopotential height, temperature, and dew point depression at the 850, 700, 500, and 300 mb mandatory pressure levels.

Since the format of the required data varies depending upon the source (i.e., WMO code, files from the NMC, or some other source), the Barnes' model provides three different data ingest routines.

The first method is to manually enter all the data. The second mode allows input from the NMC mandatory level plot files provided that they can be made available on a 5 1/4 inch floppy diskette for the IBM series of microcomputers. The final mode uses files that reside on computers which monitor the FAA 604 line and/or acquire sounding data through a link with the PROFS data ingest facility. The data in the third mode are available through the use of a 1200 baud modem over a telephone link.

A considerably more difficult problem is data coverage and completeness. The grid point interpolation scheme cannot be relied upon to give meaningful information either at the boundaries of the data domain or in areas missing data, which represent internal boundaries. The scheme is most reliable when it has a quasi-uniform distribution of data over the grid and data outside the boundaries of the grid. Barnes (1986b) pointed out that a minimum of about 75% of the observations over the data domain are required in order to obtain reliable diagnostic results.

One method for enhancing the data coverage over oceans adjacent to North America is to incorporate "bogus" data points at selected latitude/longitude points. Representative data for the bogus points can be obtained from contoured mandatory pressure level maps as provided by the NMC on AFOS. The accuracy of the bogus points needs to be no greater than ± 10 m. The data ingest procedures would have to be modified slightly to incorporate these bogus points. This was not done in the original program since the number of bogus points used would be dependent on the

selected geographical area of the grid.

Another solution to the data coverage and accuracy problem is to use the NMC grid point values obtained from LFM initial conditions or predicted height fields. For more information on this topic see Barnes (1986a).

For manual data entry the user is prompted (by messages on the screen) for the required data station by station. The order in which data are entered is important since the interpolation scheme assumes that the first element in a data file is associated with station "x", the second element is for station "y", and so on.

Format of the data input is the same as it appears on the NMC mandatory pressure charts. Three digits are entered for the height while temperature and dew point depression are entered as they appear on the charts. If the WMO coded data are used, then the tenths of values for temperature and dew point depression should also be entered for greater accuracy in subsequent lapse rate computations.

Missing data are entered as four nines (9999) for each observation that is not available or is judged to be in error. After all the data have been entered, the editing phase of the program is entered. Subprogram "EDITUAIR" allows corrections of any of the data. In the editing program instructions are given as to how to flag and correct errors. All the data entered are redisplayed on the screen for the user to verify and correct if necessary. Data must be entered as four digits for the height fields in the editing phase and not the three digit number used in the manual entry portion of the program.

As the data are displayed on the screen, an arrow may appear next to a value. This signifies that the item is outside predetermined limits. These limits are stored in an external file and the file can be edited by the user to change these limits at any time before running the program.

Upon completion of the editing (correcting) phase, the program is automatic and there isn't any more user interaction until a menu for map display is presented. The program is run by calling the required subprograms.

The subprogram "LapseRate" computes the lapse rate of temperature with pressure between the four mandatory levels based upon the input temperature data and the computed thickness of each layer. If the values are entered to the nearest degree, as are usually obtained from charts, the lapse rates can exceed dry adiabatic ($9.8^{\circ}\text{C}/\text{km}$) on some occasions. This is due to the truncation of tenths values in the input data. This will cause the magnitudes of lapse rates as seen on the contoured charts to be in error somewhat, but the relative distribution of lapse rate values can be believed. One can still see where there are centers of maximum and minimum values.

Since there are only three layers in which lapse rates can be calculated, and because the interpolation programs, for symmetry reasons, are designed to handle four variables at a time, this program will file the 850 mb temperature in addition to the three lapse rate fields.

Subprogram "MixRatio" computes the mixing ratio fields for the four pressure levels previously defined while subprogram "InterpZ" interpolates geopotential heights to grid points. The interpolation scheme used is a two-pass Barnes analysis for which the weight function parameter ($C = 63000 \text{ km}^2$ as in Barnes, 1985) is not changed for the second pass. This is a departure from the weighting scheme used by Barnes (1985) which was determined to analyze the scales of height variations that were very close to the minimum detectable signals obtainable from the U.S. rawinsonde network.

The program also interpolates the temperature lapse rate ("InterpLR") and

mixing-ratios ("InterpMR"). Then "ThicknMZ" computes the thickness and mean height for each of the three layers.

Subprogram "QVector" computes for each of the three layers the thickness temperature, geostrophic temperature advection, Q-vector components, divergence of Q, and the geostrophic frontogenesis function. Each of these diagnostic fields is computed from various combinations of gradients of geostrophic wind at the mean height of the layer and layer temperature. Layer temperature values are computed from thickness values for each layer. All gradient values are subjected to a nine-point smoothing routine before entering subsequent computations.

Subprogram "Stability" uses the mean potential temperature of each layer to compute the stability of each layer expressed as a rate of change of potential temperature with decreasing pressure. Thus, the fields should always be positive. Negative values would indicate greater than adiabatic lapse rates.

Subprogram "Vorticity" computes for each of the three layers the absolute geostrophic vorticity. The computed geopotential Laplacians are subjected to a nine-point smoothing routine. The vorticity fields are computed from the mean height fields for the three layers which have mean pressure values of 771.4, 591.6, and 387.3 mb. The mean pressure values are obtained with the equation $MP = EXP((\log(P2) + \log(P1))/2)$. In this equation MP stands for mean pressure, P1 is the lower (in height) pressure value, and P2 is the upper pressure level. Using an arithmetic mean would have been more appropriate since pressure coordinates were used in the program. However, in this case, the mean pressure values are only slightly different from what would be obtained using the arithmetic mean (775, 600, and 400 mb). For convenience, these and other fields based upon mean height values carry labels of 800, 600, and 400 mb respectively.

Both "SWLower" and "SWUpper" estimate the local lapse rate (stability) tendency in a layer. The lower layer is from 850 to 500 mb and the upper layer is from 700 to 300 mb. This overlap arises because the omega forcing is obtained at three levels. The forcing at 600 mb is used in both the lower and upper tendency computations. The computation is based upon the expression for adiabatic processes and only includes the effect of horizontal advection of stability by the geostrophic wind.

The next subprogram "StabTend" computes the stability tendency and files it in two forms. One is in the dimensions in which it is computed and the other is in dimensions more familiar to operational meteorologists, that is, $^{\circ}\text{C km}^{-1} (12\text{h})^{-1}$.

The lapse rate fields themselves are based upon reported temperature data at mandatory levels. The computed lapse rate tendency is based upon height data alone, through application of quasi-geostrophic concepts. Thus, the changes in lapse rate fields from one time to the next will not necessarily be similar to the computed tendency fields. It is unknown at this time whether their differences will reveal anything about the diabatic and ageostrophic advective processes that are not included in quasi-geostrophic theory.

The next two programs "GTLower" and "GTUpper" input the fields required to compute geopotential tendencies in the subprogram "GeopTend." The tendencies are computed as a scaled advection of vorticity.

This program also computes two forecast fields. These are height fields for $t+12$ hours and are computed from the initial height fields at 700 and 500 mb and the tendency fields for the upper and lower layers. The forecast height fields represent a gross estimate of how the height fields would change over the next few hours if geostrophic forcing were the only influence. The forecast height fields are the sum

of the initial height fields and the geopotential tendencies discussed above.

The remainder of the programs contained within the batch file deals with the graphics output. The package provided by Dr. Barnes contains two display programs. As previously mentioned twenty maps are automatically contoured on the background map. Once the maps have been generated they can be individually retrieved through the menu described below, and they can be output to a printer. Additionally, twenty other maps can be contoured from an alternate menu. These additional maps can also be sent to the printer.

Program "ContPkg" (Contour Package) contains the filenames of maps to be contoured in DATA statements. The contour intervals of each map are contained in a file named "Contour.DAT" and can be modified by the user before running the program.

The present program will blow up if too many contours are present. This is due to the limited array space available for contour points. In order to alleviate this problem another program has been added that checks the maximum and minimum values to be contoured and then ensures that the program won't try to print too many contours. If the default contour values are such that more than ten different contours values will result, then the contour interval is adjusted automatically. The number of different contour values to be drawn can be changed by adjusting one parameter in the program "AdjCntr" (Adjust Contour).

"MapView" provides the main map viewing menu for the 20 preselected fields. The individual maps can be displayed in any order and also "tagged" for later output to the printer. There is also an option that will automatically print all 20 maps. Since the maps have already been contoured and saved to disk the regeneration of these maps is almost instantaneous.

"AltMenu" is another map viewing program that can be selected from the main menu described above. The difference with the above program is that these 20 maps are contoured while the user watches instead of being retrieved from disk.

Since other maps may be desired by the user, AltMenu can be modified to give the user more maps from which to choose. This could be done by chaining another menu to the program. The only difference in this new menu program would be the contoured maps that the user could select from. The DATA statements that contain the data files to be contoured would have to be changed. This could be done as many times as desired, so that all the data generated could be contoured.

The programs described above used centered difference forms to compute derivatives at all interior points. Boundary points were evaluated by extrapolating outward from the two adjacent interior points. The four corner points used the two values on a diagonal line with the respective corner. The remainder of the boundary points used values either on a horizontal or vertical line depending on the point being evaluated.

The Barnes' program provides a picture of vertical motion at three levels in the atmosphere while the standard NGM facsimiles provide vertical motion only for the 700 mb level. Having a picture of vertical motion at three levels gives the meteorologist a more comprehensive picture of the state of the atmosphere. For instance, if there was low level upward motion and convection was possible, upper level subsidence may prevent or may cap thunderstorm development.

The Barnes' program is easily run and it is fast. The program can be run on a microcomputer which is usually available in any weather station today. After data ingest, the user can have diagnostic charts within 10 min. Since most upper air data are available between 2 and 3 h after data time, the user can have the charts

available at least 1 h before the commonly used charts are available. It is usually 4 h after data time that the first of the diagnostic or prognostic products are available in chart form.

Very little user interaction is required after data ingest. This makes it more likely that the operational meteorologist will use the program. Most of the user interaction required is obtaining and verification of the input data. The Barnes' program has defined limits on the values of input data and flags any data outside of these limits. This makes the data verification a much easier process.

All computations in the Barnes program used pressure as the vertical coordinate. The derivation section presented earlier is using a modified x, y, z coordinate system. In the x, y, p coordinate system (12) becomes

$$\nabla^2(\sigma\omega) + f^2 \frac{\partial^2 \omega}{\partial p^2} = -2(\nabla \cdot \mathbf{Q})$$

where $\sigma = -(\alpha/\theta)(\partial\theta/\partial p)$ and

$$\mathbf{Q} = \left[\frac{\partial V_g}{\partial x} \cdot \nabla \left(\frac{\partial \Phi}{\partial p} \right), \frac{\partial V_g}{\partial y} \cdot \nabla \left(\frac{\partial \Phi}{\partial p} \right) \right].$$

CHAPTER IV

CASE STUDIES

THUNDERSTORMS IN TEXAS ON 17 MARCH 1987

On 17 March 1987, eastern Texas experienced several tornadoes, hail, and high winds. The most severe weather produced by the storm system occurred between 1100 UTC and 1400 UTC (0500 and 0800 LST). This case study will look at a comparison of how the NWS prognostic maps compare with the results of the Barnes' 3-Level Q-vector program. First, a discussion of the synoptic situation will be presented.

The 1200 UTC surface map (not shown) showed a deepening 992 mb low approximately 80 km northeast of Amarillo, Texas with a warm front extending eastward through central Oklahoma and northern Arkansas. A cold front extended from the low southeastward to the Austin, Texas area and then southward to Brownsville, Texas. The surface map analysis also showed a pressure trough or possible convergence line, to the east of the cold front, that extended southward from the Wichita Falls, Texas area to Tyler, Texas and southwestward from Tyler to about 40 km west of Houston. The severe weather occurred in the vicinity of this trough line.

The NWS Radar Summary at 1035 UTC (not shown) showed a severe weather watch area that coincided with the area of the pressure trough. The severe weather watch had been issued 6 h earlier and was due to expire at 1100 UTC. The summary also showed thunderstorms throughout eastern Texas with maximum cloud tops

reaching to 45,000 ft. Subsequent radar summaries showed these thunderstorms moving eastward and the heights of maximum cloud tops increasing.

The upper air maps showed strengthening of the low pressure system in the lower and upper layers while weakening in the middle layers. The 850 mb 1200 UTC chart showed a minimum height of 1332 gpm near Amarillo, Texas which was 30 m lower than on the 0000 UTC chart on the same day. There was strong cold advection in the rear of the low. The 700 mb chart showed weak cold advection in the southern part of the low while the 500 mb chart showed mostly warm advection in the rear of the low along with an area of colder air to the southwest side of low center. The 300 mb chart had cold advection into the northwestern side of the low. Figures 6 through 9 show these charts.

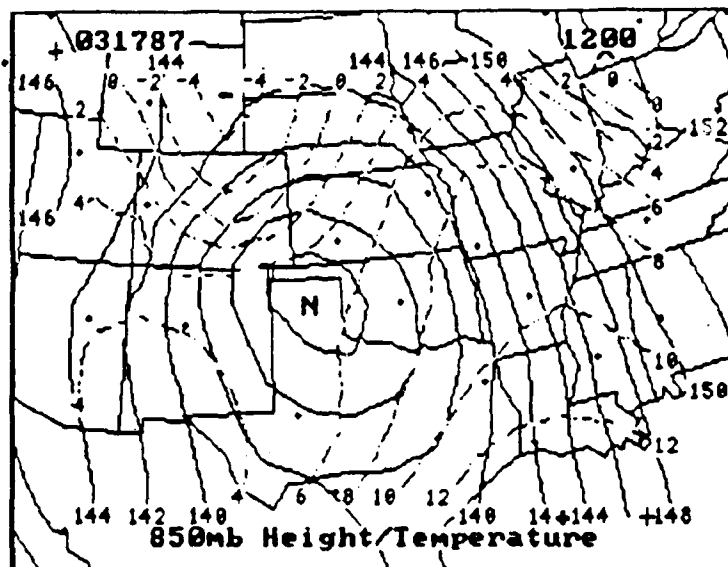


FIG. 6. 850 mb height and temperature for 1200 UTC 17 March 1987. Height (solid lines) is in dam while temperature (dashed lines) is in °C.

Concerning these and subsequent figures, contour values are only labeled on

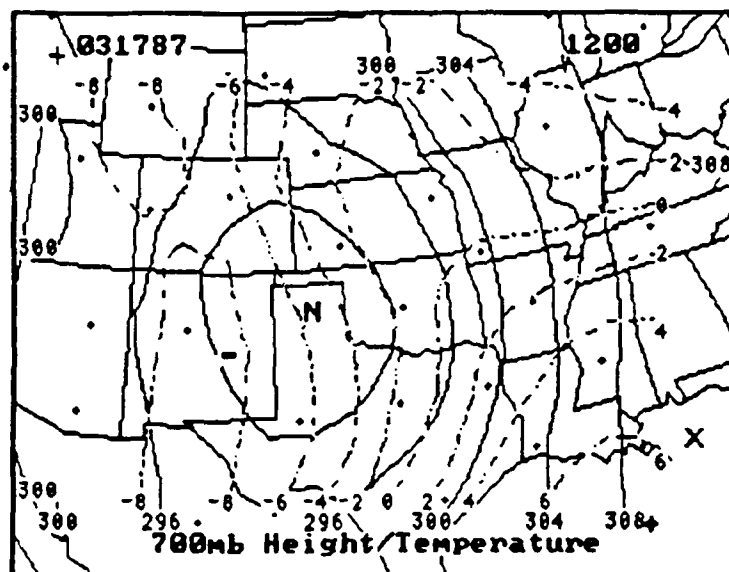


FIG. 7. 700 mb height and temperature for 1200 UTC 17 March 1987. Labelling is the same as in Fig. 6.

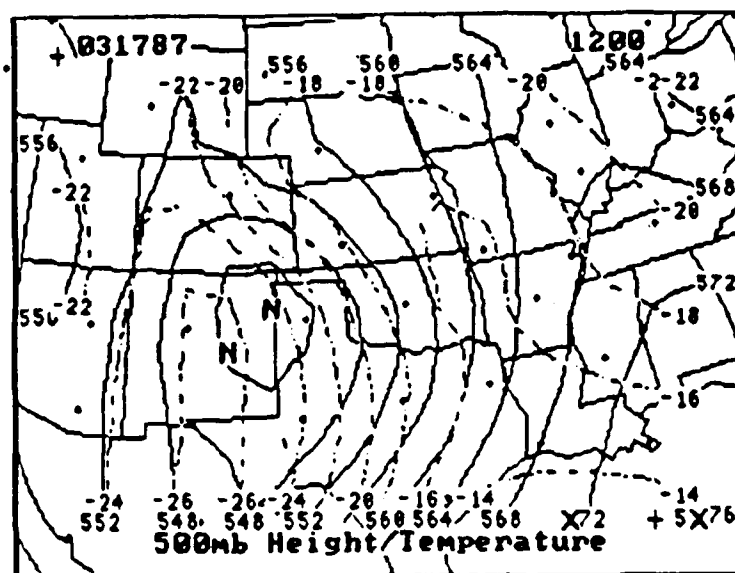


FIG. 8. 500 mb height and temperature for 1200 UTC 17 March 1987. Labelling is the same as in Fig. 6

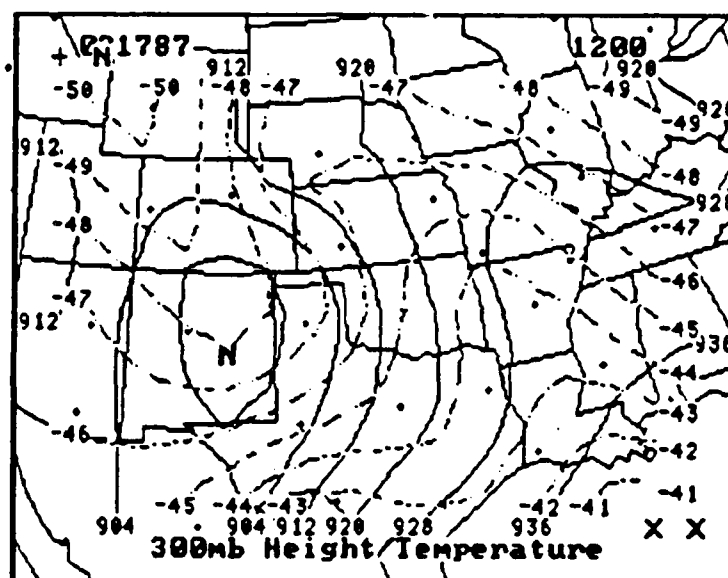


FIG. 9. 300 mb height and temperature for 1200 UTC 17 March 1987. Labelling is the same as in Fig. 6.

the edges of the charts. Maximum and minimum locations have different markings depending upon the sign of each value. If the two values are of opposite signs then maxima are labeled with an "+" and minima are labeled with a "-" while values with the same sign result in a "X" and "N" respectively. Any maximum or minimum values mentioned in the following discussion are obtained from separate numerical data files that list these values along with their grid point locations.

The NGM 36 hour forecast vorticity chart (valid 1200 UTC 17 March 1987, not shown), based upon the 0000 UTC 16 March data showed a vorticity maximum in central Texas with weak positive vorticity advection (PVA) extending into northern central Texas and negative vorticity advection (NVA) into eastern Texas. On the subsequent NGM (12 h later), the 24 h forecast vorticity chart showed the maximum in about the same location but the magnitude of the vorticity values was higher. The

vorticity advection in eastern Texas was near zero. The NGM chart, computed from the 0000 UTC 17 March data, was not available due to communication problems. This would have produced a forecast vorticity chart computed from the latest available data before the onset of severe weather.

The NGM vorticity charts are combined with the 500 mb height field forecast for the same period. The Barnes' 3-Level Q-vector program (hereafter referred to as the Barnes program) also computes vorticity but the contoured fields are combined with thickness values for the layer. The Barnes program computes vorticity for the 600 mb level and computes the thickness based upon the 700 mb and 500 mb data. Trenberth (1978) presented arguments for evaluating vertical motion based upon advection of vorticity by the thermal wind. Since the thermal wind is proportional to thickness, the user may choose to evaluate the vertical motion field using this vorticity chart. In addition to the 600 mb level, vorticity charts are also generated for the 800 mb and 400 mb levels with the appropriate thickness contours.

Figures 10 and 11 show the 600 mb vorticity field combined with the thickness field. Figure 10 is for 0000 UTC 17 March data and shows that there is PVA across northeastern Texas and into Louisiana. Figure 11 is for the 1200 UTC data and shows that the PVA across northeastern Texas has become very weak. The Barnes vorticity charts differ from the NGM charts as to a vorticity maxima location and in advection through Texas. Part of the discrepancy may be due to the NGM wind observations and predictions being subjected to smoothing algorithms.

Figures 12 and 13 show the diagnostic geopotential tendency fields at the 500 mb and the 700 mb level, measured in decameters per 12 h, at 0000 UTC. Figures 14 and 15 show the same fields 12 h later. Comparing these charts shows that, at the 700 mb level, the magnitude of the falls decreased over most of Texas over the

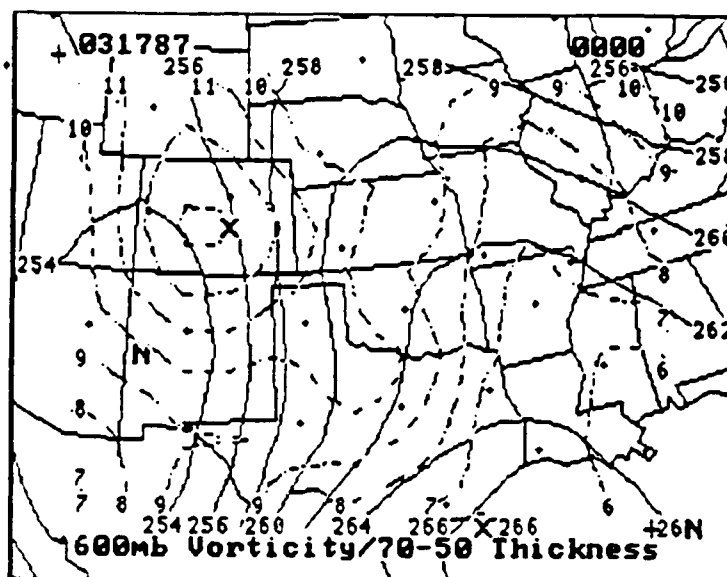


FIG. 10. 600 mb vorticity and 700-500 thickness for 0000 UTC 17 March 1987. Vorticity isopleths are dashed and the thickness (dam) are solid lines.

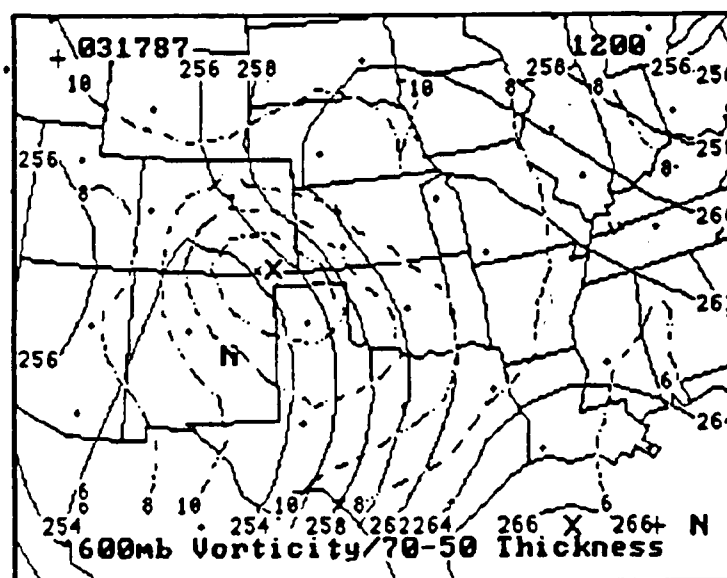


FIG. 11. 600 mb vorticity and 700-500 thickness for 1200 UTC 17 March 1987. Labelling is the same as in Fig. 10.

period from 0000 UTC to 1200 UTC. The 500 mb charts show eastern Texas under falling tendency at 0000 UTC and rising tendency 12 h later except in extreme eastern Texas. The 500 mb geopotential tendency through Texas and Louisiana is in agreement with the positive vorticity advection (PVA) pattern shown in Fig. 11. The areas of PVA coincide with the areas of falling geopotential tendency. The 700 mb negative tendency shows that the lower layers were having geopotential falls through Texas while the 500 mb charts show that there were geopotential rises in the middle layers over western Texas. The Barnes' model also computes stability tendency. The charts for the 700 mb and 500 mb layers (not shown) show that the 700 mb level was becoming more unstable and the 500 mb level was becoming more stable.

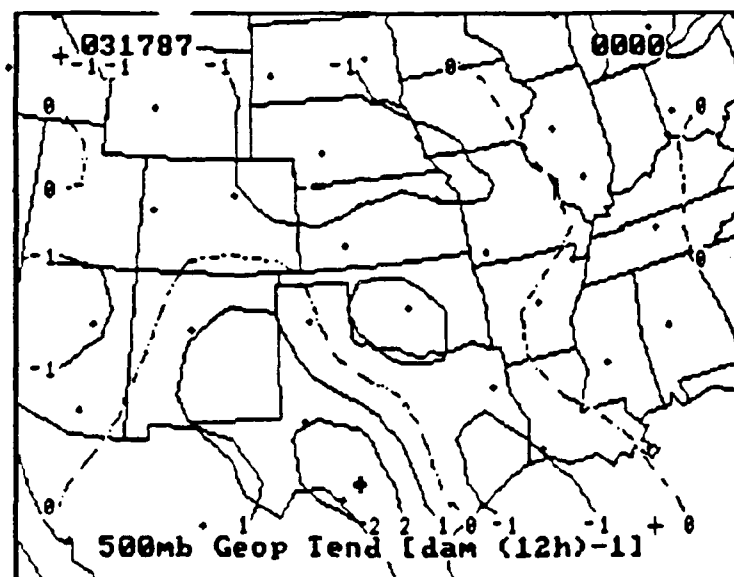


FIG. 12. 500 mb geopotential tendency for 0000 UTC 17 March 1987. Units are dam (12 h)^{-1}

The $\nabla \cdot Q$ charts for the 800 mb, 600 mb, and 400 mb layers (Figs. 16-18)

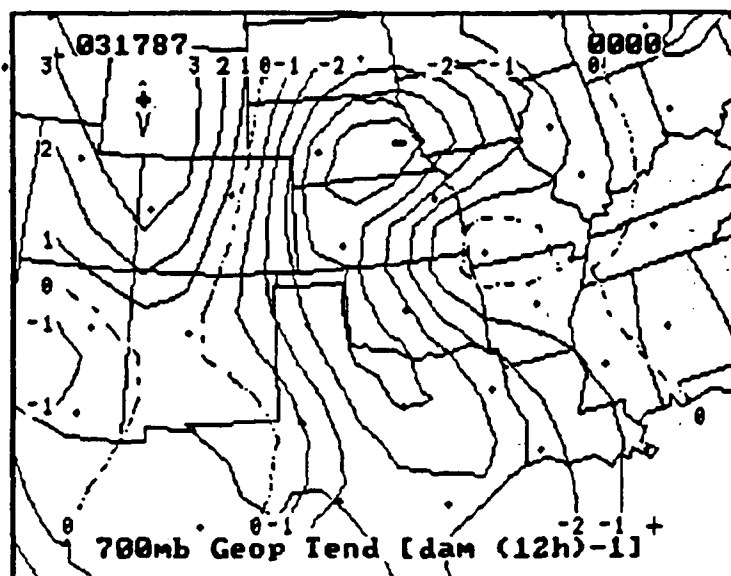


FIG. 13. 700 mb geopotential tendency for 0000 UTC 17 March 1987. Labelling is the same as in Fig. 12.

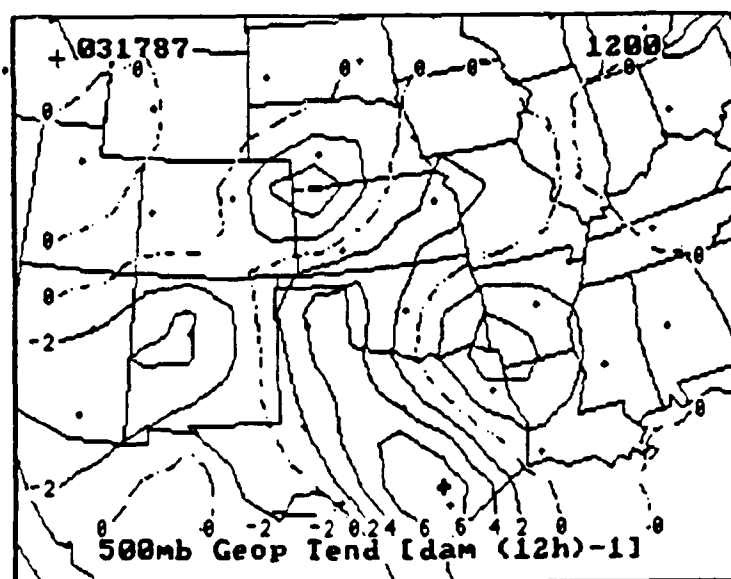


FIG. 14. 500 mb geopotential tendency for 1200 UTC 17 March 1987. Labelling is the same as in Fig. 12.

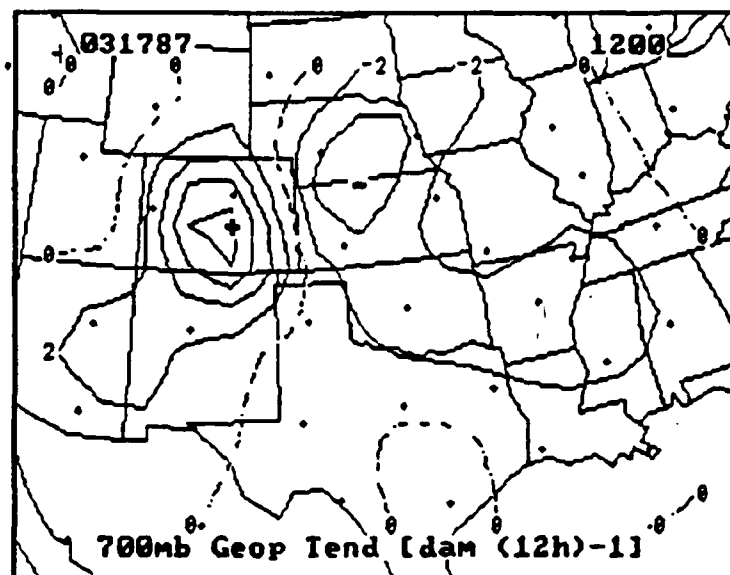


FIG. 15. 700 mb geopotential tendency for 1200 UTC 17 March 1987. Labelling is the same as in Fig. 12.

show the vertical motion associated with the storm system at 1200 UTC. The zero contour line on the 600 mb chart (Fig. 17) fairly well coincides with the surface cold front position. All three charts show relatively strong subsidence (positive values) over the western two thirds of Texas and rising motion (negative values) over the remainder of Texas. The rising motion over the eastern part of Texas, in the mid troposphere, is also consistent with the idea presented by Djurić (1969) that upward vertical motion coincides with PVA above the level and strong warm air advection below the level. The rising motion through Oklahoma, Kansas, and Nebraska can be associated with an inverted trough, extending through the center of these states, at the surface.

Water vapor, another important variable in a storm environment, is depicted as mixing ratio in Figs. 19-24. Comparing the 850 mb mixing ratio at 0000 UTC

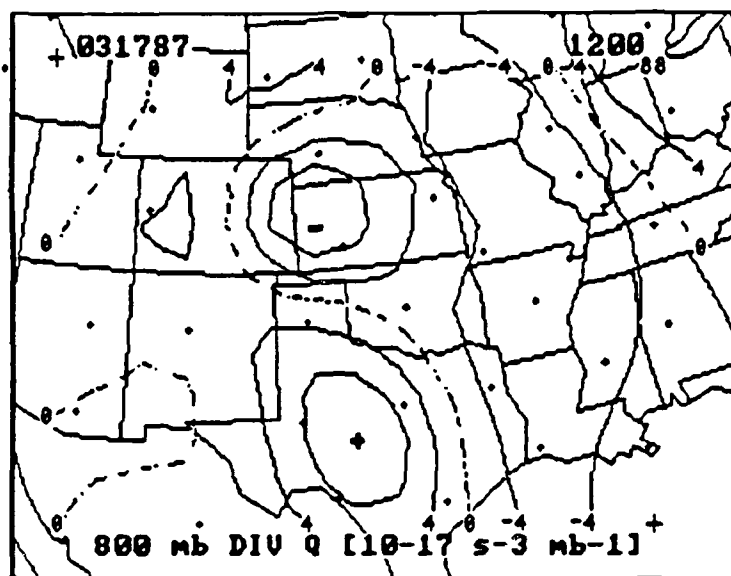


FIG. 16. 800 mb $\nabla \cdot Q$ for 1200 UTC 17 March 1987. Units are $10^{-17} \text{ s}^{-3} \text{ mb}^{-1}$.

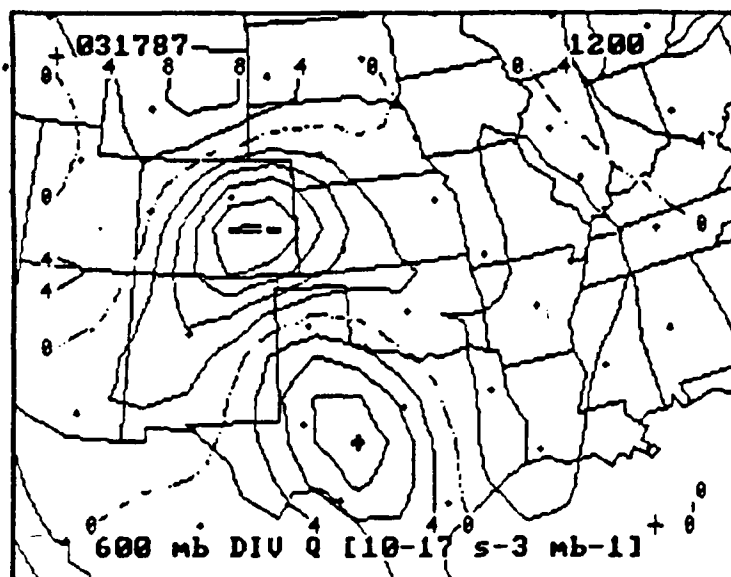


FIG. 17. 600 mb $\nabla \cdot Q$ for 1200 UTC 17 March 1987. Labelling is the same as in Fig. 16.

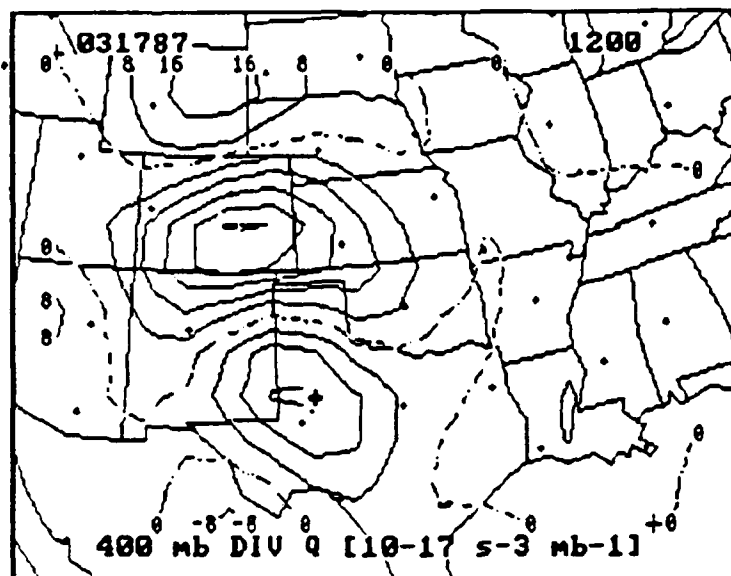


FIG. 18. 400 mb $\nabla \cdot Q$ for 1200 UTC 17 March 1987. Labelling is the same as in Fig. 16.

(Fig. 19) with 1200 UTC (Fig. 20) shows an increasingly humid and pronounced ridge over eastern Texas and Louisiana extending up through the central plains states. The water vapor patterns show the same results when comparing the 700 mb charts (Figs. 21 and 22) and the 500 mb charts (Figs. 23 and 24). In western Texas, on all the charts, the amount of moisture had decreased over the 12 h period.

The subsidence, shown on the $\nabla \cdot Q$ charts, and the decreasing humidity over western Texas showed as rapid clearing behind the front. The 36 h NGM precipitation and vertical velocity forecast charts, valid at 1200 UTC 17 March 1987 showed just the opposite. They showed continuing precipitation and lifting motion. The 48 h charts computed from the same data base showed western Texas under subsidence and decreased precipitation. The subsequent precipitation chart shows the precipitation still occurring at 1200 UTC and ending 12 h later. Since the

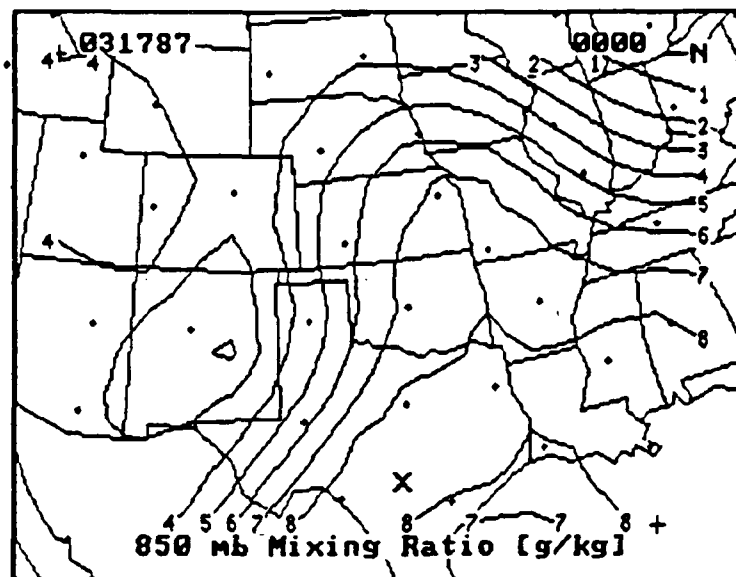


FIG. 19. 850 mb mixing ratio for 0000 UTC 17 March 1987. Units are g kg^{-1} .

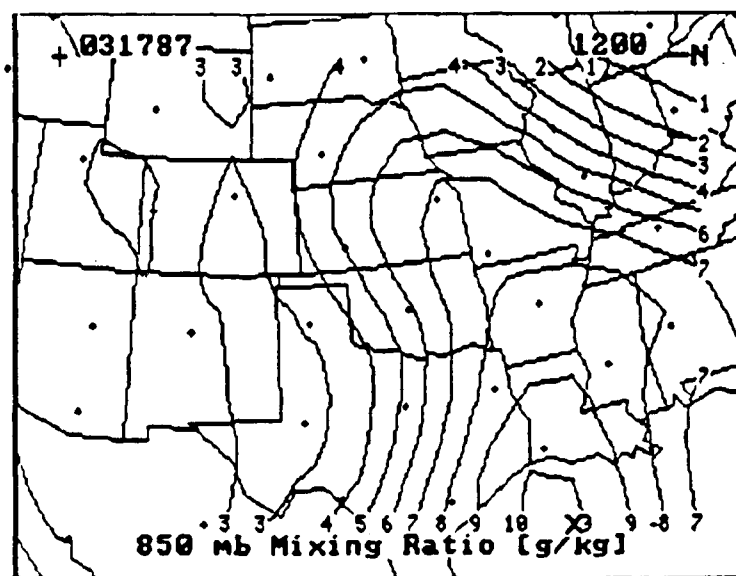


FIG. 20. 850 mb mixing ratio for 1200 UTC 17 March 1987. Labelling is the same as in Fig. 19.

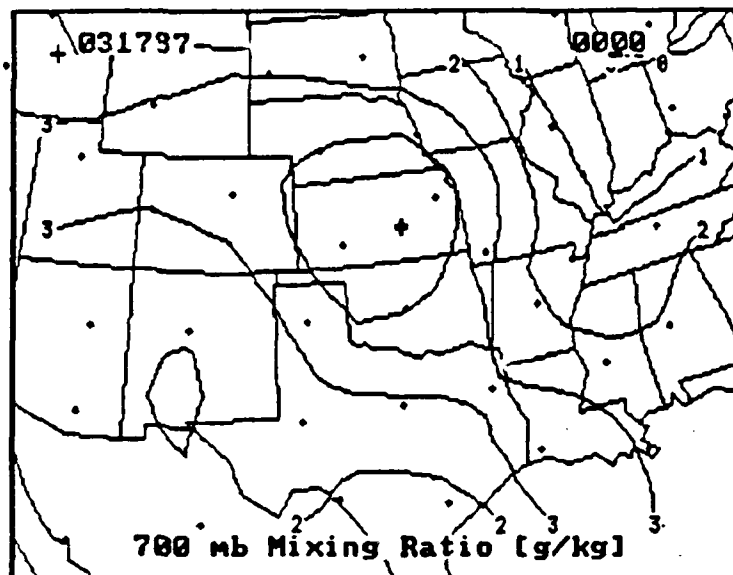


FIG. 21. 700 mb mixing ratio for 0000 UTC 17 March 1987. Labelling is the same as in Fig. 19.

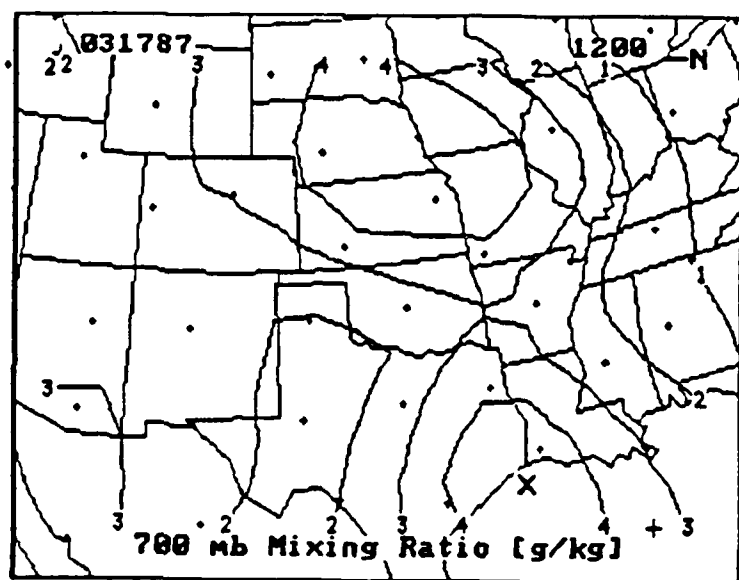


FIG. 22. 700 mb mixing ratio for 1200 UTC 17 March 1987. Labelling is the same as in Fig. 19.

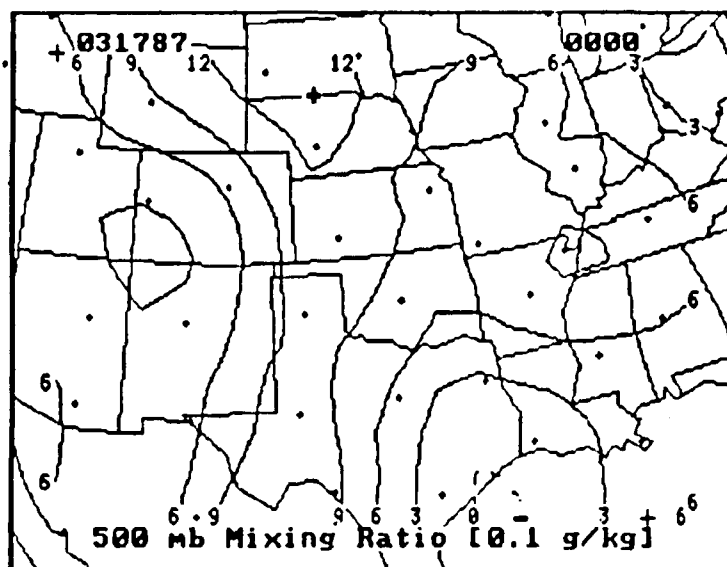


FIG. 23. 500 mb mixing ratio for 0000 UTC 17 March 1987. Units are described on the bottom of the map.

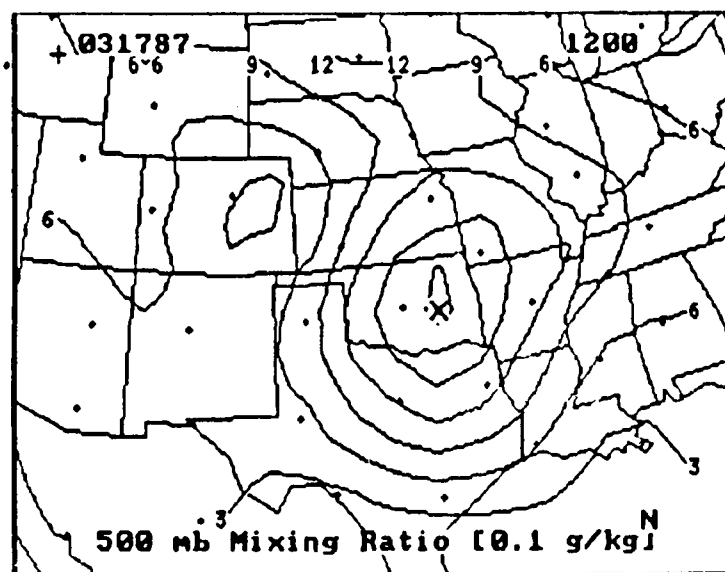


FIG. 24. 500 mb mixing ratio for 1200 UTC 17 March 1987. Labelling is the same as in Fig. 23.

NGM charts computed from the 0000 UTC 17 March 1987 data was unavailable, it is unknown if the NGM prognostic maps were still approximately 12 h slow. Based upon continuity of the NGM products it is believed that the NGM products continued to be slow in their timing.

The forecaster using the NGM products computed from the 0000 UTC 17 March data, for example, could have compared these products to the Barnes model results. If, as assumed, the NGM continued the precipitation over western Texas, then the forecaster could have adjusted his use of the NGM products based upon the quasi-geostrophic forcing as depicted by the Barnes program and comparison with available satellite pictures. The forecaster would have seen the decreasing precipitation over western Texas and the enhanced storm environment over eastern Texas. The rising motion and increased humidity ahead of the front helped enhance the storm environment in that area.

From the Q and temperature charts (Figs. 25-27) the $\nabla \cdot Q$ maps, previously discussed, can be constructed. The Barnes' program labels the charts with part of the title as "Thickness Temperature." The contoured field is a computed temperature based upon the thickness of the layer. There is rising motion where the Q -vectors converge and conversly, subsidence where they diverge.

Figure 26 shows the convergence of the Q -vectors over eastern Texas and western Louisiana. This corresponds to the rising motion depicted in the same area in Fig. 17. Western Texas shows $\nabla \cdot Q > 0$ which corresponds to the subsidence area in Fig. 17.

Comparing the direction of the Q -vector with respect to the temperature contours yields the GFF. When the Q -vector has a component pointing from colder air toward warmer air, the potential temperature gradient is enhanced and a positive

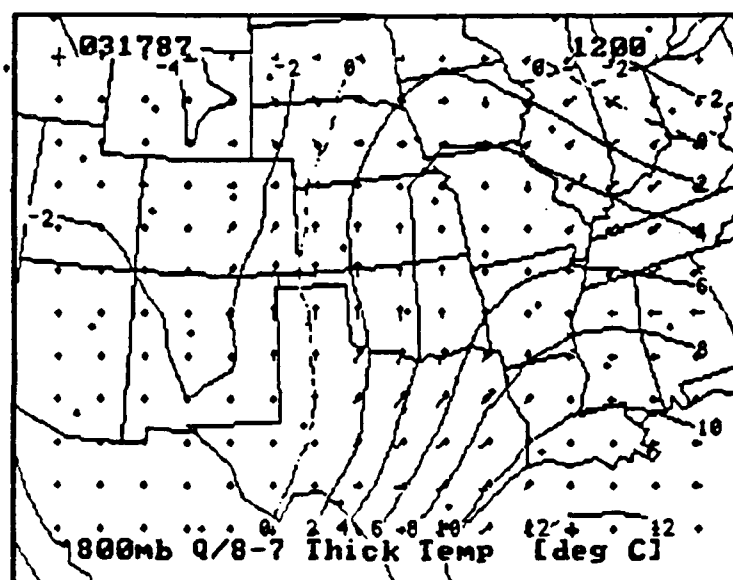


FIG. 25. 800 mb Q and temperature for 1200 UTC 17 March 1987. The temperature, computed from thickness of the layer from 850 mb to 700 mb, is in $^{\circ}\text{C}$. Arrows represent the direction and magnitude of Q .

GFF results. A positive GFF signifies frontogenesis. A component of Q from warm to cold air indicates a geostrophic frontolytic situation (negative GFF).

Figures 28–30 show the resulting GFF for the 800 mb, 600 mb, and 400 mb levels. Comparing Fig. 25 with Fig. 28 shows that across central Texas at 800 mb the Q -vectors point from cold to warm and have a corresponding positive GFF. In this case the motion was tending to intensify the thermal gradient in the vicinity of the frontal system. A comparison of Fig. 26 with Fig. 29 shows that at 600 mb there is a weak component of motion from cold to warm across central Texas and therefore a relatively weak positive area of GFF in the same region. At the 400 mb level the northeastern part of Texas has a positive GFF.

One must be careful when interpreting the GFF. In this situation the GFF is acting to maintain the frontal circulations and not to support the actual formation of

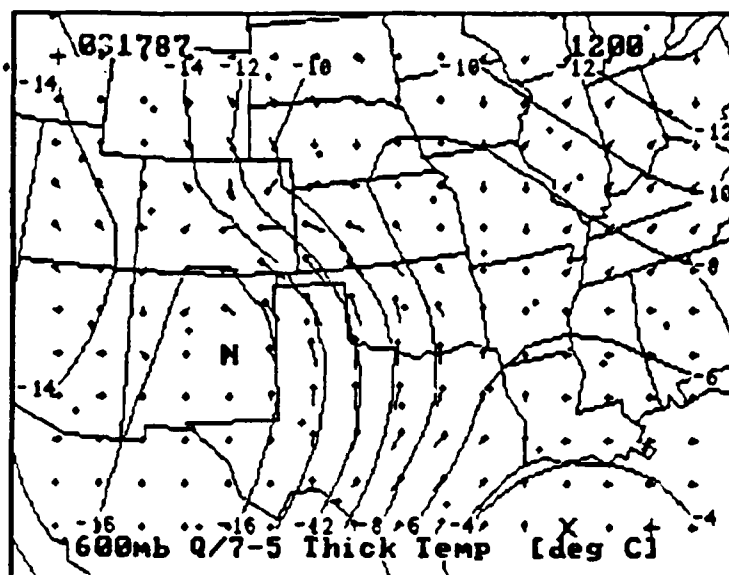


FIG. 26. 600 mb Q and temperature for 1200 UTC 17 March 1987. Labelling is the same as in Fig. 25.

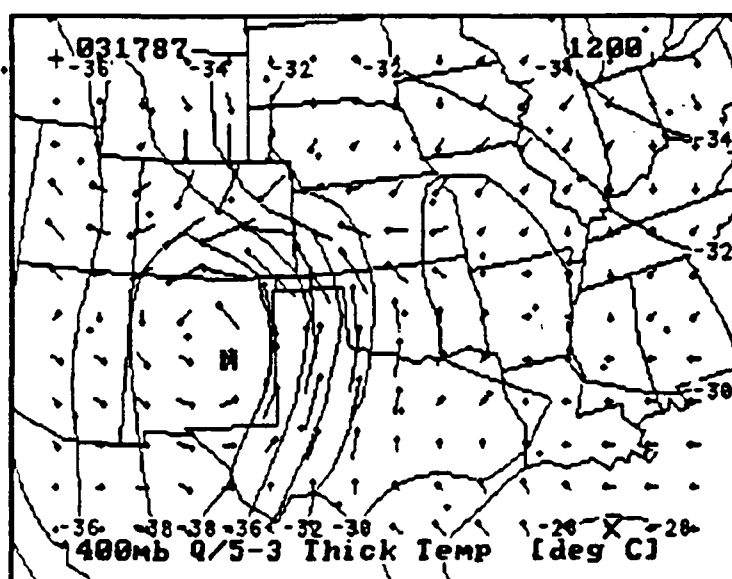


FIG. 27. 400 mb Q and temperature for 1200 UTC 17 March 1987. Labelling is the same as in Fig. 25

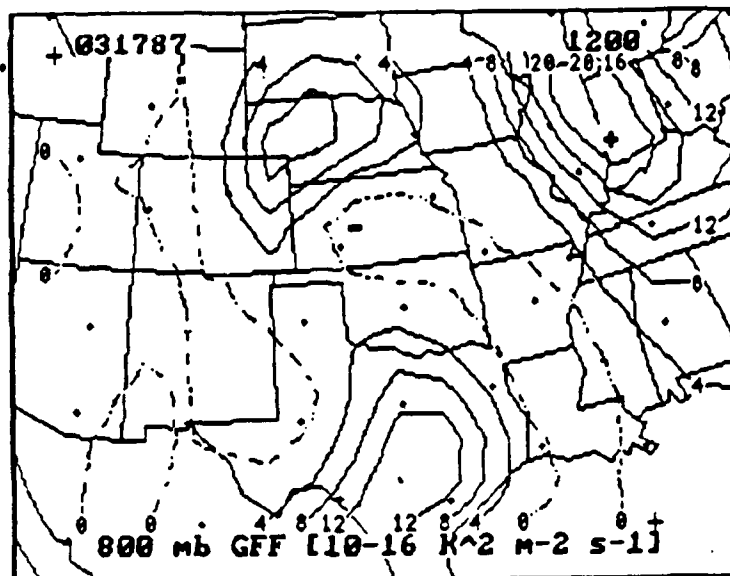


FIG. 28. 800 mb GFF for 1200 UTC 17 March 1987. Units are $10^{-16} \text{ K}^2 \text{ m}^{-2} \text{ s}^{-1}$

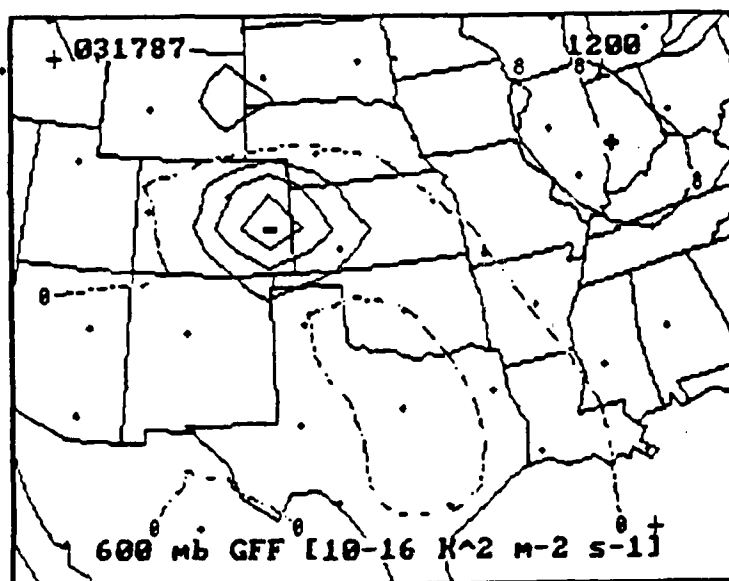


FIG. 29. 600 mb GFF for 1200 UTC 17 March 1987. Labelling is the same as in Fig. 28.

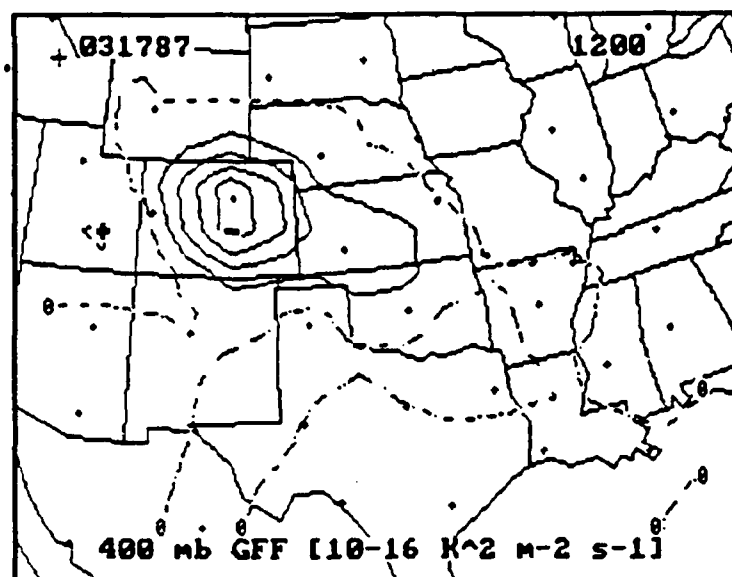


FIG. 30. 400 mb GFF for 1200 UTC 17 March 1987. Labelling is the same as in Fig. 28.

a front. As Holton (1979 pp. 240–242) pointed out, the quasi-geostrophic equations are invalid beyond the initial stages of frontogenesis. Barnes (1985) hypothesized that geostrophic frontogenesis might provide the organizing environment in which the ageostrophic frontogenetic components operate more effectively.

The charts in this case show that the front was intensifying in the lower layers and that there was rising motion at each level over eastern Texas. The strong vertical motion combined with the influx of water vapor allowed the thunderstorms to produce the severe weather.

Now that it has been shown how the Barnes' diagnostic charts corresponded with the prognostic charts, one may look closer at how the diagnostic charts related to the actual synoptic conditions at the time. This will consist of comparing the $\nabla \cdot \mathbf{Q}$ charts with the NWS Radar Summaries. To start this procedure, a chart

can be used with the appropriate segment of the U.S. outlined and marked off in 1° latitude/longitude increments. The NWS Radar Summary can be overlaid onto this chart. The only concern is with the outline of the precipitation area. The last preliminary step is to overlay the $\nabla \cdot \mathbf{Q}$ charts for the 800, 600, and 400 mb levels onto the same chart. Unless otherwise specified in the following discussion, the contour drawn is the $\nabla \cdot \mathbf{Q} = 0$ contour. The overlaid chart, constructed for 1200 UTC 17 March 1987, is shown in Fig. 31. For the sake of clarity, the 1° latitude/longitude increments are omitted in Fig. 31.

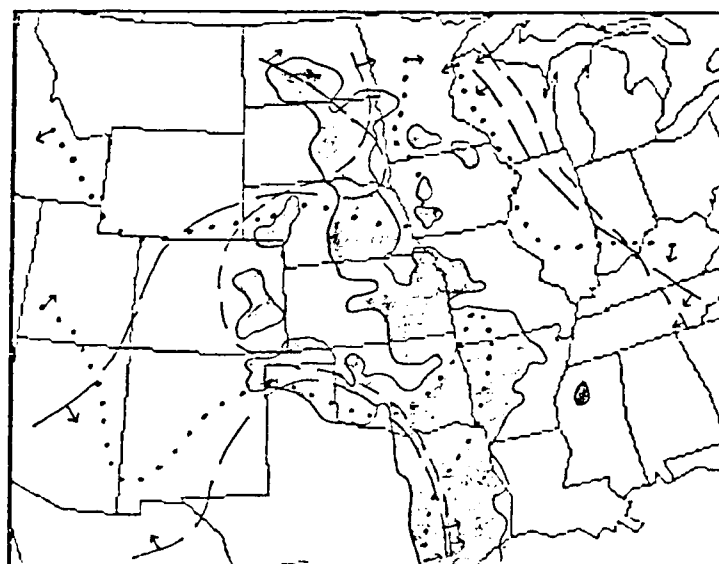


FIG. 31. Composite chart for 1200 UTC 17 March 1987. Precipitation (shaded area) is overlaid with $\nabla \cdot \mathbf{Q}$ computed at 800 mb (short dashed lines), 600 mb (long dashed lines), and 400 mb (dotted lines). The arrows represent the side of the contour with $\nabla \cdot \mathbf{Q} < 0$.

A comparison will be made of implied vertical motion with the precipitation areas by counting the latitude/longitude points that are within regions meeting the desired criteria. Two sets of comparisons will be made using the composite map.

The first set of comparisons determines the ratio of the number of points with precipitation and lifting to the total number of precipitation points. This is done for the 800, 600, and 400 mb levels. Also, a ratio of the number of points with precipitation and lifting at any level to the total number of precipitation points will be determined. For convenience this final ratio will be called a composite ratio.

The second set of comparisons determines the ratio of the number of implied subsidence points that are precipitation free to the total number of implied subsidence points. As above, this will be done for each of the three levels. Finally a composite ratio will be determined by comparing the precipitation free subsidence points to number of points with implied subsidence at every level.

Table 1 shows the results of the two sets of comparisons. The first line is for the comparisons dealing with precipitation and lifting. The second line is for the precipitation free areas and subsidence comparisons. There are two numbers in each column of both lines. The first number represents the number of points meeting the required criteria and the second number represents the total number of points considered.

Looking at Table 1 in more detail, it is seen in the precipitation case that at 800 mb, 68 out of 85 precipitation points are in a area of implied lifting. Rounding this to the nearest percentage, this is 80%. The percentages for each of the ratios in Table 1 is given in Table 2.

It is seen, from Tables 1 and 2, that the results for each level were almost the same. It is also seen, from the composite map (Fig. 31), that this is a fairly homogeneous area of precipitation. Why weren't the figures in Tables 1 and 2 higher? Part of the reason may be due to the smoothing and interpolation schemes used in the evaluation of the $\nabla \cdot Q$ charts.

TABLE 1. Ratios of precipitation points with lifting over total precipitation points and the ratios of precipitation free subsidence points over total subsidence points for 1200 UTC 17 March 1987. For each group of two numbers the first number represents the number of points meeting the required criteria and the second number is the number of total points considered. The composite column considers points with lifting at any level.

	800 mb	600 mb	400 mb	Composite
PCPN	68/85	69/85	66/85	77/85
NO PCPN	224/241	165/181	197/216	141/148

TABLE 2. Percentages for data in TABLE 1.

	800 mb	600 mb	400 mb	Composite
PCPN	80	81	78	91
NO PCPN	93	91	91	95

An additional test was performed on the precipitation case for 800 mb in order to determine if the percentage shown in Table 2 was statistically significant. The confidence interval (99%) for a binomial experiment was found to be $< 60\%$. The result shown in Table 2 is that 80% of the precipitation areas had upward motion at the 800 mb level and therefore the result is statistically significant. This was expected since low level upward motion is expected in precipitation regions.

The second line, in Tables 1 and 2, shows a higher percentage of subsidence areas being precipitation free. Since, in this case, the precipitation points within subsidence areas were near the $\nabla \cdot \mathbf{Q} = 0$ contour, one may possibly infer that the precipitation was abating in these areas. For stronger magnitudes of subsidence (i.e. $\nabla \cdot \mathbf{Q} \geq 4 \times 10^{-17} s^{-3} mb^{-1}$) the subsidence areas are precipitation free. To see this compare the values of $\nabla \cdot \mathbf{Q}$ in Figs. 16-18 with the precipitation area in Fig. 31.

Another set of comparisons was made in order to ascertain the relationship between values of $\nabla \cdot Q$ and precipitation. The first comparison was to see what proportion of the upward vertical motion area had precipitation. Once again, the $\nabla \cdot Q = 0$ contour is used.

The second comparison was as above, except with use of a stronger value of vertical motion, i.e. a critical value of $\nabla \cdot Q \leq -2 \times 10^{-17} s^{-3} mb^{-1}$. Results of these two sets of comparisons are shown in Tables 3 and 4. Table 3 shows the ratios while Table 4 shows the percentages.

TABLE 3. Ratio of number of precipitation points within lifting regions to total number of lifting points for 1200 UTC 17 March 1987. Each column shows the ratio within the range of $\nabla \cdot Q$ given. The composite column considers points with lifting at any level. Units of $\nabla \cdot Q$ are $10^{-17} s^{-3} mb^{-1}$.

$\nabla \cdot Q$	800 mb	600 mb	400 mb	Composite
≤ 0	68/289	69/349	66/314	77/382
≤ -2	64/190	67/235	44/207	77/283

TABLE 4. Percentages for data in TABLE 3.

$\nabla \cdot Q$	800 mb	600 mb	400 mb	Composite
≤ 0	24	20	21	20
≤ -2	34	29	21	26

The results, in Tables 3 and 4, show that using $\nabla \cdot Q \leq -2$ gives higher percentage values at the 800 and 600 mb levels than those obtained using $\nabla \cdot Q \leq 0$. In this case, the 400 mb level did not show a significant change. The composite results were determined using upward vertical motion at any level and showed a overall increase in percentage with $\nabla \cdot Q \leq -2$.

One may infer, from these comparisons, that if adequate moisture is available, then, areas with higher values of upward vertical motion have an increased probability of precipitation occurring. This was the case with the results obtained using values of implied lifting at the 800 and 600 mb levels.

In this case the Barnes program showed that the computed quasi-geostrophic forcing was in agreement with the atmospheric dynamics at the time. It is believed, based upon continuity from one data base time to the next, that the NGM was likely to continue being 12 h slow in its precipitation and vertical velocity forecasts. However, the NGM products were not available to verify this supposition. The Barnes program results can be used to help diagnose the current state of the atmosphere and can be used in diagnosing the performance of other products. The Barnes program shows more detail in the vertical structure of the atmosphere than the NGM products. Vertical motion is implied at three levels with the Barnes program while the NGM only gives vertical motion at one level. The results of the Barnes program are available sooner than the NGM products. The Barnes program results are available approximately 10 min after acquisition of the required upper air data.

THUNDERSTORMS IN THE CENTRAL PLAINS ON 4 JUNE 1980

For this case study the Q-vector charts are examined for correspondence with a low level jet (LLJ) and the initiation of a large scale thunderstorm, or possible MCC, event over central Nebraska and also over northwestern North Dakota. This is done in order to check the Q-vector results under a different synoptic situation than the previous case study.

The synoptic situation at 0000 UTC on 4 June 1980 had a quasi-stationary warm front extending from a low pressure center over northwestern Nebraska, southeastward through central Missouri. The interest in this case study is in the cold air ahead of the warm front (Fig. 32).

The 850 mb geopotential and temperature field (not shown) showed strong baroclinicity with the isotherms being 180° out of phase with the geopotential contours throughout the central plains states. The wind field at 850 mb showed a LLJ which extended from the panhandle of Texas northward through central Nebraska (shown in Fig. 32).

The 700 mb, 500 mb, and 300 mb charts (not shown) for the same time showed that the isotherms at these levels were for the most part in phase with the geopotential contours. Thus the atmosphere was equivalently barotropic at and above 700 mb.

The thunderstorm activity over North Dakota started at about 2000 UTC on 3 June 1980 while the activity over central Nebraska started at about 2300 UTC. These times were determined by using available satellite photographs and radar summaries. By 0500 UTC on 4 June 1980 each of the storm areas covered two states. The thunderstorms over North Dakota propagated to the east-northeast

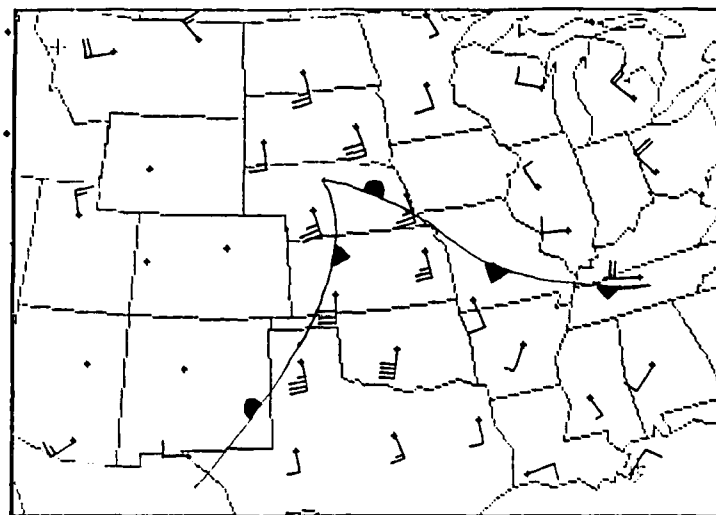


FIG. 32. 850 mb wind field and surface frontal position for 0000 UTC 4 June 1980. Wind speed is in knots. Long feathers represent 10 kt and short feathers represent 5 kt. Surface frontal position is from the NMC surface chart for the same time.

while the Nebraska storms propagated to the east.

Referring back to the LLJ at 850 mb (Fig 32.), the maximum wind was actually not at this level. Plotting a vertical sounding for Oklahoma City showed that the maximum winds were occurring at about 900 mb. There was an inversion just above the 850 mb layer.

It is seen in Fig. 33, that there is an area of strong Q-vector convergence near the axis of the southward motion. This produces the area of maximum upward motion over Nebraska and Kansas seen in Fig. 34. This upward motion area coincides with the Nebraska thunderstorm system. Over North Dakota there is a large value of lifting which may help to explain the development of the thunderstorm there.

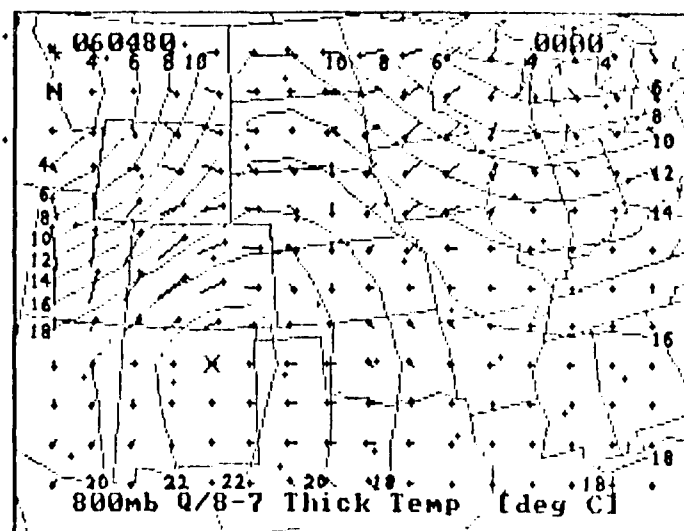


FIG. 33. 800 mb Q and temperature for 0000 UTC 4 June 1980. Arrows represent the direction and magnitude of Q . Temperature is given in $^{\circ}C$.

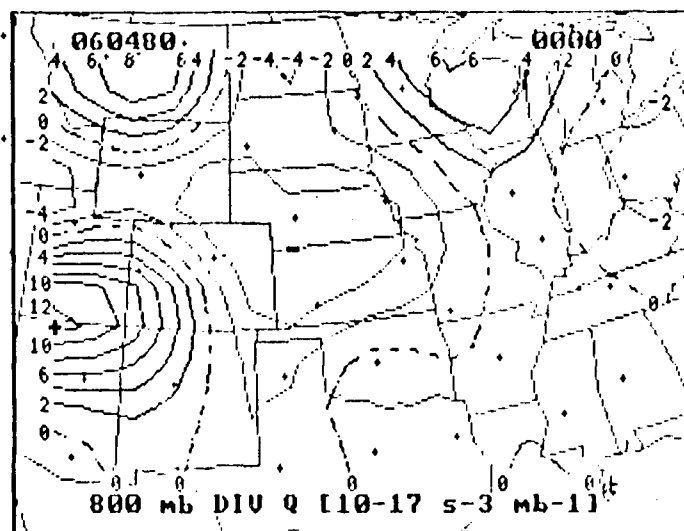


FIG. 34. 800mb $\nabla \cdot Q$ for 0000 UTC 4 June 1980. Units are $10^{-17} \text{ s}^{-3} \text{ mb}^{-1}$.

The 600mb $\nabla \cdot Q$ chart (Fig. 35) for 0000 UTC 4 June shows that there was

upward motion over the same areas but that the magnitude was smaller. From this decrease in $\nabla \cdot Q$ over North Dakota, Nebraska, and Kansas, one may infer that the forcing which contributed to the storm environment was strongest in low levels and probably associated with the LLJ.

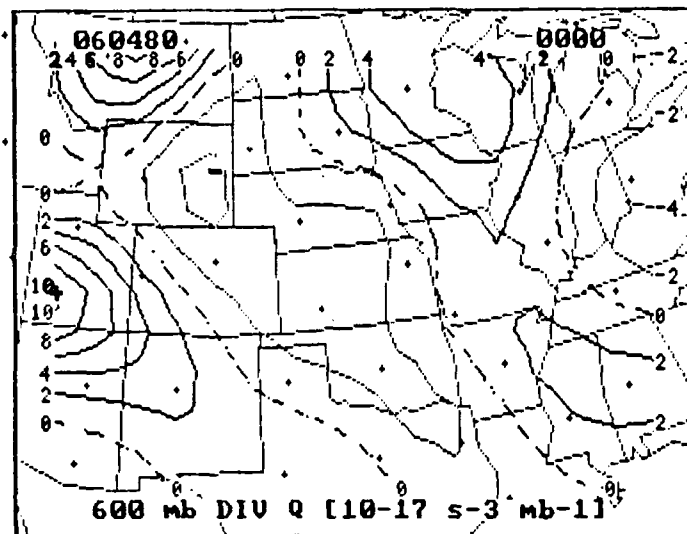


FIG. 35. 600 mb $\nabla \cdot Q$ for 0000 UTC 4 June 1980. Labelling is the same as in Fig. 34.

The 800 mb GFF chart (Fig. 36) for 0000 UTC 4 June shows that the flow, depicted in Fig. 33, has enhanced the thermal gradient over the Minnesota and Iowa area. The strong positive GFF area is on the cold side of the warm front and one may assume that the circulation in that area was favorable for maintenance or enhancement of the front.

Twelve hours later, at 1200 UTC, both storms continued to grow in size. The 800 mb Q-vector chart (Fig. 37) for 1200 UTC 4 June 1980 shows that the convergence area has moved eastward over the preceding 12 h. The convergence

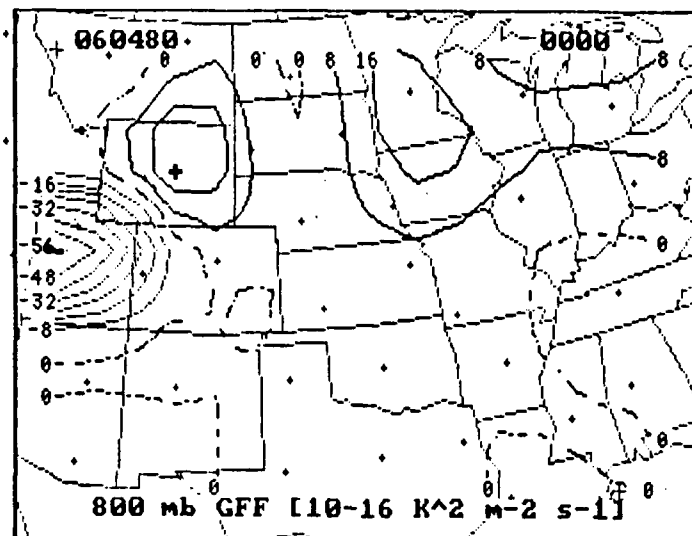


FIG. 36. 800 mb GFF for 0000 UTC 4 June 1980. Units are described on the bottom of the map.

area is now over the western Iowa area and this coincides with the eastward translation of the northern portion of the LLJ during the same period. The Q -vectors pointing southward still mark the area of the LLJ.

The 800 mb $\nabla \cdot Q$ chart for 1200 UTC 4 June 1980 (Fig. 38) shows the area of upward motion has propagated eastward into the same region and that the magnitudes of $\nabla \cdot Q$ have increased. The upward motion area over North Dakota has grown in size while the subsidence area over Minnesota is now confined to northern Minnesota and has weakened over the 12 h period.

The 800 mb GFF chart, for 1200 UTC 4 June 1980, (Fig. 39) shows that the gradient of positive values over Iowa, eastern Nebraska, and northern Missouri has increased. From this increase one may expect that the front now has a more vigorous circulation and is more intense.

By 0000 UTC on 5 June 1980 all the storms discussed were diminishing in

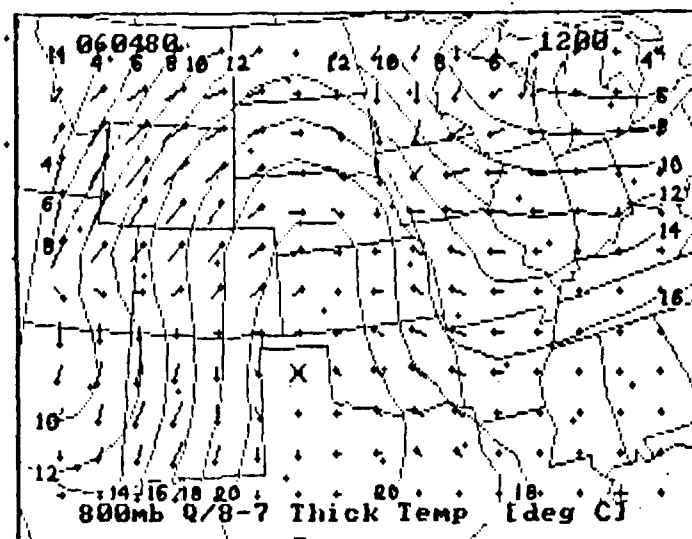


FIG. 37. 800 mb Q and temperature for 1200 UTC 4 June 1980. Labelling is the same as in Fig. 33.

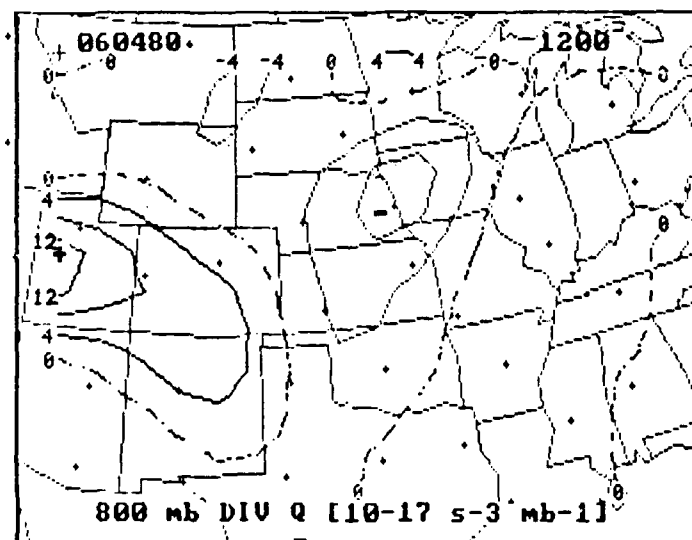


FIG. 38. 800 mb $\nabla \cdot Q$ for 1200 UTC 4 June 1980. Labelling is the same as in Fig. 34.

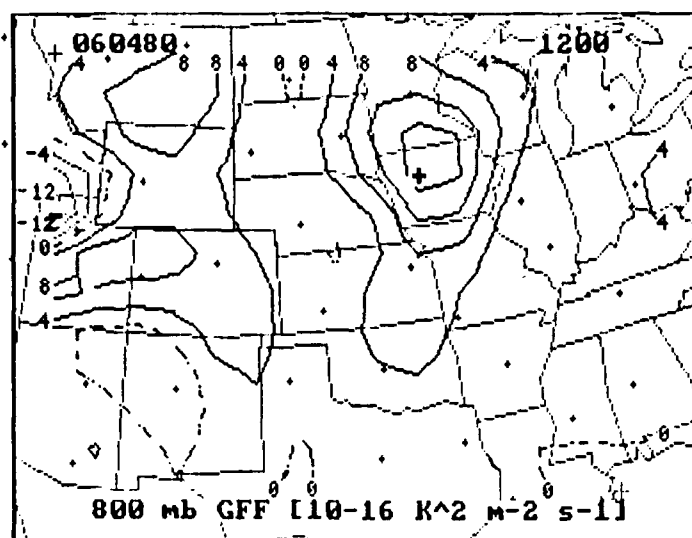


FIG. 39. 800 mb GFF for 1200 UTC 4 June 1980. Labelling is the same as in Fig. 36.

size and intensity. The LLJ at this time was also weakening. The 800 mb Q-vector chart, for this time, (Fig. 40) shows smaller Q-vectors. This implies that the corresponding flow was weaker and thus the vertical motion as a result of the convergence of Q was weaker. With a decrease in lifting the storm should weaken.

The Q-vector convergence, shown in Fig. 41, also shows smaller values over the Nebraska and Iowa area. The magnitude of the convergence increased over Oklahoma and eastern portion of the Texas panhandle. Coincidentally a thunderstorm developed over the northern Texas area and lasted for a few hours.

The positive GFF (Fig. 42) values for 0000 UTC on 5 June 1980 have decreased in magnitude. This was primarily due to the smaller magnitude of the Q-vectors over Iowa (Fig. 40) and thus there was weaker ageostrophic motion over Iowa.

So far, this case study has shown that by using the Q-vector diagnostic charts

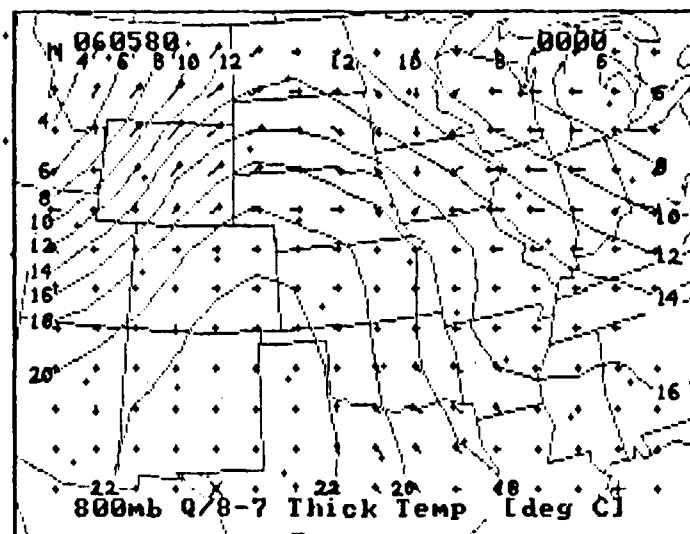


FIG. 40. 800 mb Q and temperature for 0000 UTC 5 June 1980. Labelling is the same as in Fig. 33.

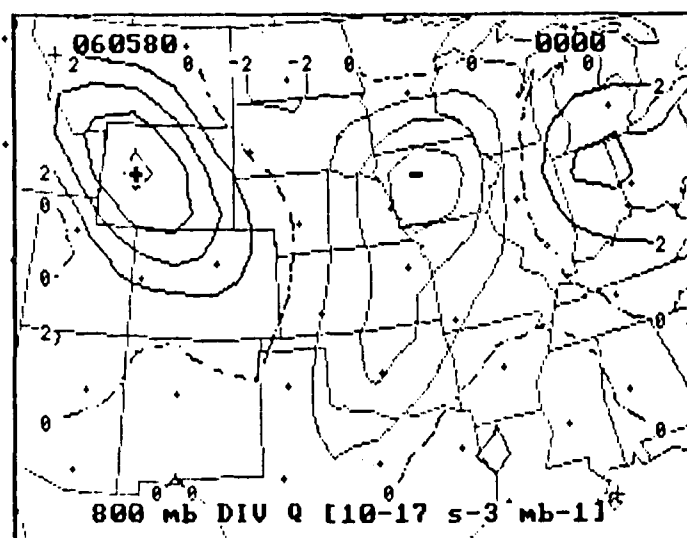


FIG. 41. 800 mb $\nabla \cdot Q$ for 0000 UTC 5 June 1980. Labelling is the same as in Fig. 34.

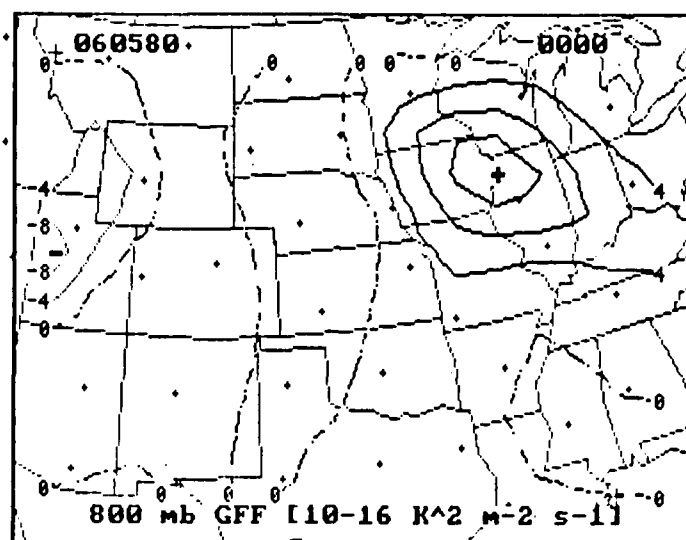


FIG. 42. 800 mb GFF for 0000 UTC 5 June 1980. Labelling is the same as in Fig. 36.

an operational meteorologist could have seen the changes in atmospheric circulations and made an improved forecast accordingly. For example, the increase in values of the upward motion and also GFF could have led the forecaster to conclude that the thunderstorm activity would have continued over Iowa. It has also been seen that the strongest upward vertical motion was in the vicinity of the LLJ.

In this case study the time period considered was from 0000 UTC 4 June 1980 through 0000 UTC 5 June 1980. In order to check the correspondence between different combinations of precipitation and vertical motion for both the mature as well as the decaying stages of a thunderstorm, the time period considered will be extended to 0000 UTC 6 June 1980.

A set of composite charts was constructed using the same methods described in the previous case study. The resultant composite chart with $\nabla \cdot \mathbf{Q}$ for 0000

UTC 4 June 1980 and the NWS Radar Summary for 0135 UTC 4 June 1980 are depicted in Fig. 43. Figure 43 shows that we do not have a large continuous (homogeneous) precipitation area. Here we have relatively small and somewhat separated precipitation areas. This is also true for the composite charts created for the remaining four time periods under study. Each time period is 12 h later than the previous one. Since these charts are similar to Fig 43, they are not shown. We are primarily interested in the ratios evaluated from these charts.

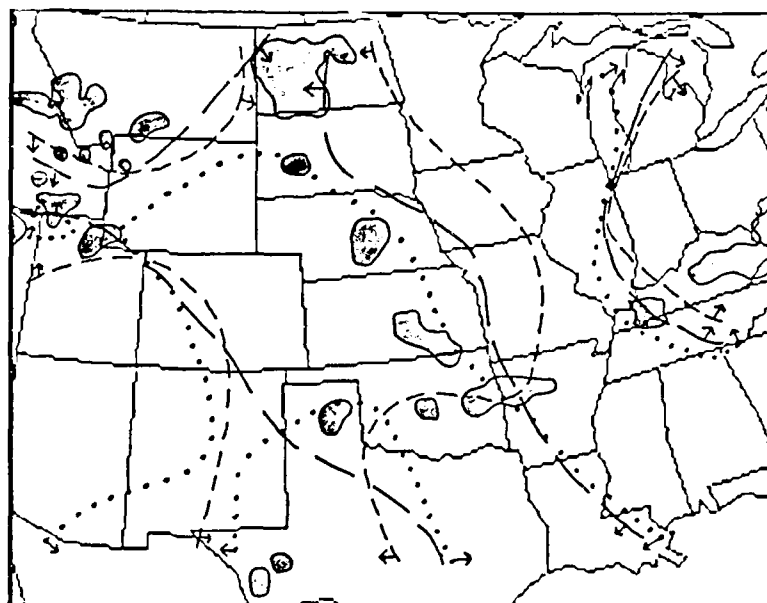


FIG. 43. Composite chart for 0000 UTC 4 June 1980. Precipitation (shaded area) is overlaid with computed values of $\nabla \cdot \mathbf{Q} \leq 0$ for the 800 mb (short dashed lines), 600 mb (long dashed lines), and 400 mb (dotted lines) levels. The arrows represent the side of the contour with $\nabla \cdot \mathbf{Q} < 0$.

Concerning the tables that follow, the Time/Date column shows the time of the Radar Summary chart used. The Radar Summary charts are compared with the $\nabla \cdot \mathbf{Q}$ charts computed for the nearest time. In all but the first case, in each table, there is a 25 min difference in time between the $\nabla \cdot \mathbf{Q}$ chart and the corresponding

Radar Summary chart. In the first case there is a 95 min time difference. The 2335 UTC 3 June 1980 NWS Radar Summary chart was not available for some unknown reason.

The first set of comparisons determines the ratio of number of precipitation points with implied lifting to the total number of precipitation points. This is done for the 800, 600, and the 400 mb levels. A composite ratio is also determined by considering lifting at any level.

Table 5 shows the results of determining these ratios. Table 6 shows the percentages for the data in Table 5. The 800 mb level shows, in Table 6, the highest percentages, of precipitation points having implied lifting motion, in four out of five cases. The 600 mb level, in three out of five cases, shows a relatively large drop in percentages from values obtained at the 800 mb level. In all five cases, the 400 mb level had the lowest percentages. For the composite column, the percentages remained fairly high. At this stage we may infer that the precipitation was being caused by primarily lower to middle tropospheric effects.

TABLE 5. Ratio of precipitation points with lifting over total number of precipitation points for case 2. The composite column considers points that have lifting at any level.

Time/Date	800 mb	600 mb	400 mb	Composite
0135 UTC 4 JUNE	29/41	30/41	20/41	35/41
1135 UTC 4 JUNE	33/50	22/50	21/50	37/50
2335 UTC 4 JUNE	52/72	32/72	25/72	60/72
1135 UTC 5 JUNE	32/51	30/51	20/51	36/51
2335 UTC 5 JUNE	33/55	24/55	18/55	46/55

For this case study, we are not seeing the same consistency, between levels, that we saw with the previous case study. Part of the reason may be due to the

TABLE 6. Percentages for data in TABLE 5.

Time/Date	800 mb	600 mb	400 mb	Composite
0135 UTC 4 JUNE	71	73	49	85
1135 UTC 4 JUNE	66	44	42	74
2335 UTC 4 JUNE	72	44	35	83
1135 UTC 5 JUNE	63	59	39	71
2335 UTC 5 JUNE	60	44	33	84

geographical location of the precipitation in the northwestern portion of the grid. Notice, in Fig. 43, that the northwestern portion of the grid is located over Idaho and western Montana. This area contains a portion of the Rocky Mountain range. Therefore some of the precipitation, in this area, may be due to terrain effects and not due to quasi-geostrophic effects. Referring back to the composite chart (Fig. 43), it can be seen that if the precipitation areas over the northwestern area of the grid are disregarded, then the percentage of precipitation areas having upward vertical motion would increase dramatically at every level. Since it is known that the atmosphere does not react only to quasi-geostrophic effects, the precipitation area in question will not be disregarded. In all five time periods discussed, the majority of the precipitation occurring within subsidence areas is in the Idaho/Montana area.

The confidence interval (99%) for a binomial experiment was evaluated for the 800 mb values shown in Table 6. In every case the percentages shown in Table 6 were found to be statistically significant. This was expected since precipitation is usually associated with low level upward motion.

Next the ratio of the subsidence areas that are precipitation free is examined. For this comparison, Table 7 shows the tabulated data while Table 8 shows the percentages for the data in Table 7. The composite column, in each of these tables, the subsidence is determined in areas that show subsidence at every level.

TABLE 7. Ratio of number of subsidence points that are precipitation free over the total number of subsidence points for case 2. The composite column considers points with subsidence occurring at every level.

Time/Date	800 mb	600 mb	400 mb	Composite
0135 UTC 4 JUNE	241/253	259/270	287/308	177/183
1135 UTC 4 JUNE	205/222	170/198	216/245	108/121
2335 UTC 4 JUNE	225/245	268/308	259/306	157/169
1135 UTC 5 JUNE	268/287	256/277	263/294	180/195
2335 UTC 5 JUNE	223/242	270/279	322/340	155/164

TABLE 8. Percentages for data in TABLE 7.

Time/Date	800 mb	600 mb	400 mb	Composite
0135 UTC 4 JUNE	95	96	93	97
1135 UTC 4 JUNE	92	86	88	89
2335 UTC 4 JUNE	92	87	85	93
1135 UTC 5 JUNE	93	92	89	92
2335 UTC 5 JUNE	92	97	95	95

Table 8 shows that the results remained relatively constant through each time period and each level. These results are very similar to the corresponding results in the previous case study (see Tables 1 and 2). It can be inferred that the computed subsidence areas are relatively accurate since these areas are almost precipitation free, as expected.

Two more sets of comparisons are made to conclude this study. Both sets determine the ratio of precipitation points within a area of lifting to the total number of implied lifting points. The difference, in these two sets, is the value of $\nabla \cdot \mathbf{Q}$ used. The first set considers vertical motion with computed values of $\nabla \cdot \mathbf{Q} \leq 0$ while the second set considers values of $\nabla \cdot \mathbf{Q} \leq -2 * 10^{-17} s^{-3} mb^{-1}$.

The results using $\nabla \cdot \mathbf{Q} \leq 0$ are shown in Tables 9 and 10. Table 9 shows the

evaluated data and Table 10 shows the percentages of the data in Table 9. For these tables, the composite column considers lifting at any level. As seen in these tables the ratio of the total lifting area having precipitation is relatively small.

TABLE 9. $\nabla \cdot \mathbf{Q} \leq 0$ versus precipitation. Each column shows the ratio of the number of lifting points having precipitation to the total number of lifting points. The composite column considers lifting at any level.

Time/Date	800 mb	600 mb	400 mb	Composite
0135 UTC 4 JUNE	29/277	30/260	20/222	35/347
1135 UTC 4 JUNE	33/308	22/332	21/285	37/409
2335 UTC 4 JUNE	52/285	32/222	25/224	60/361
1135 UTC 5 JUNE	32/243	30/253	20/236	36/335
2335 UTC 5 JUNE	33/288	24/251	18/190	46/366

TABLE 10. Percentages for data in TABLE 9.

Time/Date	800 mb	600 mb	400 mb	Composite
0135 UTC 4 JUNE	10	12	9	10
1135 UTC 4 JUNE	11	7	7	9
2335 UTC 4 JUNE	18	14	11	17
1135 UTC 5 JUNE	13	12	8	11
2335 UTC 5 JUNE	11	10	9	13

Tables 11 and 12 show the ratio of the total lifting area having precipitation. Lifting values used for this comparison are $\nabla \cdot \mathbf{Q} \leq -2 * 10^{-17} s^{-3} mb^{-1}$. Table 11 shows the evaluated data while Table 12 shows the percentages for the data in Table 11. Comparing Table 10 with Table 12 shows that the 800 mb percentages increased with $\nabla \cdot \mathbf{Q} \leq -2 * 10^{-17} s^{-3} mb^{-1}$. This is also true, in three out of five cases, for the 600 mb level. The 400 mb level showed a drop in percentages with the stronger lifting value in all five cases. Finally, the composite column shows a increase in

TABLE 11. $\nabla \cdot \mathbf{Q} \leq -2 * 10^{-17} s^{-3} mb^{-1}$ versus precipitation. This table is the same as Table 9 except for the value of $\nabla \cdot \mathbf{Q}$ used in determining the ratios.

Time/Date	800 mb	600 mb	400 mb	Composite
0135 UTC 4 JUNE	18/137	12/106	7/112	22/204
1135 UTC 4 JUNE	17/154	7/135	9/192	20/290
2335 UTC 4 JUNE	24/104	10/55	4/51	28/156
1135 UTC 5 JUNE	30/87	21/77	0/77	30/152
2335 UTC 5 JUNE	28/165	14/104	11/76	29/199

TABLE 12. Percentages for data in TABLE 11.

Time/Date	800 mb	600 mb	400 mb	Composite
0135 UTC 4 JUNE	13	11	6	11
1135 UTC 4 JUNE	11	5	5	7
2335 UTC 4 JUNE	21	18	8	18
1135 UTC 5 JUNE	34	27	0	20
2335 UTC 5 JUNE	17	13	6	15

percentages for four out of five cases. It is again inferred that the precipitation may have been due to primarily lower to middle tropospheric forcing.

One can also imply, from Tables 10 and 12, that given adequate water vapor, quasi-geostrophic effects in the lower troposphere are more likely to produce precipitation than the same effects in the upper troposphere. Normally, an operational meteorologist will look for adequate water vapor and lifting to produce precipitation. The meteorologist usually looks for these parameters in the lower to middle troposphere. Therefore, it is seen that the above results are consistent with concepts commonly used by a meteorologist.

CHAPTER V

CONCLUSIONS

This paper gives a review of the Barnes' diagnostic model and its application in operational work. The examples presented demonstrate the usefulness of \mathbf{Q} , $\nabla \cdot \mathbf{Q}$, and GFF in a variety of weather situations.

In the case of the thunderstorms through eastern Texas, the Barnes' diagnostic charts outperformed the much more elaborate NGM products. The \mathbf{Q} -vector, $\nabla \cdot \mathbf{Q}$, and GFF charts correctly showed the quasi-geostrophic forcing for the frontal system moving through Texas. The NGM products were approximately 12 h slow in movement of the front and associated precipitation. The forcing depicted in the Barnes program results was also conducive to enhancement of the thunderstorms and subsequent severe weather. This case study also showed additional charts produced by the Barnes program that may be of use in operational meteorology. These include mixing ratio, geopotential tendency, and stability tendency charts. Mixing ratio charts are computed for four levels in the atmosphere while the geopotential and stability tendency charts are computed for three levels. This gives the forecaster a more detailed picture of the vertical structure of the atmosphere.

The second case study showed the location and subsequent spreading of an MCC in detail. The depicted forcing agreed with thunderstorm and front locations. In this case the low level forcing was shown to be more significant than middle and upper level forcing. The 800 mb $\nabla \cdot \mathbf{Q}$ chart showed the strongest convergence magnitudes and these occurred in the vicinity of the LLJ.

For both case studies the precipitation field was for the most part within an area

of computed lifting. The computed subsidence areas were primarily precipitation free. This simple check lends credence to the computed $\nabla \cdot \mathbf{Q}$ values. Also shown in both cases was that precipitation was more likely to occur as the magnitude of the convergence of \mathbf{Q} increased in the 800 and 600 mb levels. GFF gave a good indication of frontal intensity and subsequent development.

Overall, the Barnes program provides a more detailed picture of the quasi-geostrophic effects in the atmosphere. The \mathbf{Q} -vector charts give information on the horizontal ageostrophic motion which in turn gives an indication of the frontal circulations. The \mathbf{Q} -vector field overlaid with a layer temperature field graphically shows where the thermal field is being enhanced or weakened and thus gives a reliable picture of frontal development. The magnitude of the \mathbf{Q} -vector is proportional to the strength of the horizontal ageostrophic wind below the level at which \mathbf{Q} is computed.

The \mathbf{Q} -vector formulation of the omega equation and the corresponding charts are valuable tools when used in conjunction with other diagnostic and prognostic products. As is well known, there can be differences between different charts. Using a program such as the Barnes program gives the meteorologist another tool to help ascertain the current state of the atmosphere. Once the current state of the atmosphere has been determined then the product differences can be resolved and a more accurate forecast can be made.

Two potential problems arise when comparing the NWS Radar Summary charts with the $\nabla \cdot \mathbf{Q}$ charts. First the radar summary charts differ in time from the $\nabla \cdot \mathbf{Q}$ charts by about 30 min. Second, the radar summary charts are an estimate of the actual precipitation fields. The radar summary charts are a composite of the many radar reports received by the NWS and some of the lighter precipitation falling may

not be seen by the radar.

Future research efforts could possibly use the actual radar reports to plot the areas of precipitation and then make the same types of comparisons. Another research recommendation is to determine the relationship between the amount of atmospheric water vapor, $\nabla \cdot Q$ values, and precipitation. The final recommendation is for a frequency distribution study of the values of $\nabla \cdot Q$ and precipitation. This frequency distribution study may provide a critical value of $\nabla \cdot Q$ that infers probable precipitation. This would be similar to the relationship between stability indices such as K-Index or Total-Totals values and convective activity.

REFERENCES

- Barnes, S. L., 1985: Omega guidance as a supplement to LFM MOS guidance in weakly forced convective situations., *Mon. Wea. Rev.*, **113**, 2122-2141.
- , 1986a: The limited-area fine-mesh model and quasi-geostrophic theory: A disturbing case study., *Wea. Forecasting*, **1**, 89-96.
- , 1986b: On the accuracy of omega diagnostic computations., *Mon. Wea. Rev.*, **114**, 1664-1680.
- Cahir, J. J., J. M. Norman and D. A. Lowry, 1981: Use of a real-time computer graphics system in analysis and forecasting., *Mon. Wea. Rev.*, **109**, 485-500.
- Djurić, D., 1969: Note on estimation of vertical motion by the omega equation., *Mon. Wea. Rev.*, **97**, 902-904.
- Doswell, Charles A., 1987: The distinction between large scale and mesoscale contribution to severe convection: A case study example., *Wea. Forecasting*, **2**, 3-16.
- Durran, Dale R., and Leonard W. Snellman, 1987: The diagnosis of synoptic-scale vertical motion in an operational environment., *Wea. Forecasting*, **2**, 17-31.
- Holton, J. R. 1979: *An Introduction to Dynamic Meteorology*, 2nd ed., International Geophysics Series, Vol 23, Academic Press, 391 pp.

Hoskins, B. J., I. Draghici and H. C. Davies, 1978: A new look at the Ω -equation., *Quart. J. Roy. Meteor. Soc.*, **104**, 31-38.

Hoskins, B. J., and M. A. Pedder, 1980: The diagnosis of middle latitude synoptic development., *Quart. J. Roy. Meteor. Soc.*, **106**, 707-719.

Sutcliffe, R. C., 1947: A contribution to the problem of development., *Quart. J. Roy. Meteor. Soc.*, **73**, 370-383.

Trenberth, K. E., 1978: On the interpretation of the diagnostic quasi-geostrophic omega equation., *Mon. Wea. Rev.*, **106**, 131-137.

VITA

Charles Arthur LeMay [REDACTED],
Maryland to Gilbert and Daphne LeMay. He graduated from Gen. William M. Moultrie High School in 1970 and entered the United States Air Force in November of 1971. Through off-duty education programs and subsequent enrollment at the Baptist College in Charleston, S.C., he received his B.S. in Mathematics in December of 1981. While attending Baptist College he was enrolled in the Air Force Reserve Officer Training Corps and upon graduation was commissioned a second lieutenant in the USAF. He then attended Texas A&M University from January to December of 1982 where he completed the Basic Meteorology Program. Upon completion of this program he served as the Wing Weather Officer and unit forecaster at Myrtle Beach Air Force Base in Myrtle Beach, S.C. for a period of one year. Then he transferred to Traben-Trarbach, West Germany, where he served as a team chief at the United States Army in Europe Forecast Unit. There he provided weather support to U.S. and NATO military forces in Europe from February 1983 until July 1986. In August of 1986 he returned to Texas A&M University to work on a Masters of Science degree in Meteorology.

[REDACTED]
[REDACTED]
G. [REDACTED]